Journal of Computational Physics 380 (2019) 191–211

Contents lists available at ScienceDirect

Journal of Computational Physics

www.elsevier.com/locate/jcp

Fast algorithms for integral formulations of steady-state radiative transfer equation

Yuwei Fan [a,*], Jing An [b], Lexing Ying [a,b]

[a] Department of Mathematics, Stanford University, Stanford, CA 94305, United States of America
[b] Institute for Computational and Mathematical Engineering, Stanford University, Stanford, CA 94305, United States of America

ARTICLE INFO

Article history:
Received 30 January 2018
Received in revised form 19 December 2018
Accepted 26 December 2018
Available online 9 January 2019

Keywords:
Fast algorithm
Radiative transfer
Fredholm integral equation
Recursive skeletonization
FFT
Anisotropic scattering

ABSTRACT

We investigate integral formulations and fast algorithms for the steady-state radiative transfer equation with isotropic and anisotropic scattering. When the scattering term is a smooth convolution on the unit sphere, a model reduction step in the angular domain using the Fourier transformation in 2D and the spherical harmonic transformation in 3D significantly reduces the number of degrees of freedoms. The resulting Fourier coefficients or spherical harmonic coefficients satisfy a Fredholm integral equation of the second kind. We study the uniqueness of the equation and proved an a priori estimate. For a homogeneous medium, the integral equation can be solved efficiently using the FFT and iterative methods. For an inhomogeneous medium, the recursive skeletonization factorization method is applied instead. Numerical simulations demonstrate the efficiency of the proposed algorithms in both homogeneous and inhomogeneous cases and for both transport and diffusion regimes.

© 2018 Elsevier Inc. All rights reserved.

1. Introduction

The radiative transfer equation (RTE) is the primary equation for describing particle propagation in many different fields, such as neutron transport in reactor physics [31,10], light transport in atmospheric radiative transfer [27], heat transfer [25] and optical imaging [24,36]. In this paper, we focus on the steady state radiative transfer equation with possibly anisotropic scattering

$$\begin{aligned} \boldsymbol{v}\cdot\nabla_{\boldsymbol{x}}\Phi(\boldsymbol{x},\boldsymbol{v})+\mu_t(\boldsymbol{x})\Phi(\boldsymbol{x},\boldsymbol{v}) &= \mu_s(\boldsymbol{x}) \fint_{\mathbb{S}^{d-1}} \sigma(\boldsymbol{x},\boldsymbol{v}\cdot\boldsymbol{v}')\Phi(\boldsymbol{x},\boldsymbol{v}')\,\mathrm{d}\boldsymbol{v}' + f(\boldsymbol{x}), \quad \text{in } \Omega\times\mathbb{S}^{d-1}, \\ \Phi(\boldsymbol{x},\boldsymbol{v}) &= 0, \quad \text{on } \Gamma_-, \end{aligned} \tag{1.1}$$

where the quantity $\Phi(\boldsymbol{x},\boldsymbol{v})$ denotes the photon flux that depends on both space $\boldsymbol{x}$ and angle $\boldsymbol{v}$, and $f(\boldsymbol{x})$ is the light source. $\Omega\in\mathbb{R}^d$ is a bounded Lipschitz domain, $\mathbb{S}^{d-1}$ is the unit sphere in $\mathbb{R}^d$, $\fint$ is the average integral, and $\Gamma_- = \{(\boldsymbol{x},\boldsymbol{v})\in\partial\Omega\times\mathbb{S}^{d-1} : \boldsymbol{n}(\boldsymbol{x})\cdot\boldsymbol{v}<0\}$ with $\boldsymbol{n}(\boldsymbol{x})$ being the outer unit normal vector at $\boldsymbol{x}$. The scattering kernel $\sigma(\boldsymbol{x},\boldsymbol{v}\cdot\boldsymbol{v}')\geq 0$ satisfies $\fint_{\mathbb{S}^{d-1}}\sigma(\boldsymbol{x},\boldsymbol{v}\cdot\boldsymbol{v}')\,\mathrm{d}\boldsymbol{v}'=1$. The transport coefficient $\mu_t=\mu_a+\mu_s$ measures the total absorption at $\boldsymbol{x}$ due on both the physical absorption quantified by the term μ_a and the scattering phenomenon quantified by the term μ_s. To simplify the discus-

* Corresponding author.
E-mail addresses: ywfan@stanford.edu (Y. Fan), jingan@stanford.edu (J. An), lexing@stanford.edu (L. Ying).

https://doi.org/10.1016/j.jcp.2018.12.014
0021-9991/© 2018 Elsevier Inc. All rights reserved.

sion, we only consider the vacuum boundary condition and assume that the source term f is independent of the angular variable $\boldsymbol{v}$. General boundary condition and source terms will be discussed in Section 4.

Numerical methods for solving the RTE can be categorized into two groups: (a) the probabilistic approaches, for example Monte Carlo methods [4,9,19] and (b) the deterministic schemes based on differential-integral equations. In the past decades, many deterministic methods have been proposed, including different discretization in the spatial and angular domains [1,3, 26,8,37,13,15,18,2,32] and various preconditioned iterative schemes [28,30,16].

However, numerical solutions of RTE still face several challenging issues. One of them is the high dimensionality of the photon flux $\Phi(\boldsymbol{x}, \boldsymbol{v})$, which depends on both the spatial variable $\boldsymbol{x}$ and the angular variable $\boldsymbol{v}$. For a d-dimensional problem, the photon flux therefore depends on a total of $d + (d-1) = 2d-1$ variables. Another issue is the computation of the scattering term

$$S(\boldsymbol{x}, \boldsymbol{v}) = \mu_s(\boldsymbol{x}) \fint_{\mathbb{S}^{d-1}} \sigma(\boldsymbol{x}, \boldsymbol{v} \cdot \boldsymbol{v}')\Phi(\boldsymbol{x}, \boldsymbol{v}')\, \mathrm{d}\boldsymbol{v}'. \tag{1.2}$$

Due to the $(d-1)$-dimensional integral in the above formula, a naive computation of the RTE is a $d + (d-1) + (d-1) = (3d-2)$-dimensional problem. This poses a significant bottleneck for efficient numerical simulations of the RTE.

Recently in [32], the authors studied the isotropic scattering case (i.e. $\sigma(\boldsymbol{x}, \boldsymbol{v} \cdot \boldsymbol{v}') \equiv 1$) and converted the RTE into a Fredholm integral equation of the second kind of the *mean local density* $\fint_{\mathbb{S}^{d-1}} \Phi(\boldsymbol{x}, \boldsymbol{v})\, \mathrm{d}\boldsymbol{v}$. One can then directly solve the mean local density first without the solution of the photon flux Φ. When $\Phi(\boldsymbol{x}, \boldsymbol{v})$ is needed, then it can be computed easily by solving a transport equation with a known right hand side. In [14], the authors studied the RTE in a plane-parallel geometry and converted it to a Fredholm integral equation by expanding the scattering term into Legendre polynomials.

Inspired by the approaches of [14,32], in this work we propose integral formulations and fast algorithms for the RTE with smooth isotropic or anisotropic scattering. The primary assumption of the algorithm is that the angular dependence of the scattering term $S(\boldsymbol{x}, \boldsymbol{v})$ can be represented efficiently using a small number of modes. One can convert the RTE into a Fredholm equation of the second kind of these modes, thus achieving a significant model reduction. As in [32], once the scattering term $S(\boldsymbol{x}, \boldsymbol{v})$ is resolved, applying existing methods (e.g. [15,18]) to the following transport equation with the right hand side known gives the photon flux $\Phi(\boldsymbol{x}, \boldsymbol{v})$

$$\begin{aligned} \boldsymbol{v} \cdot \nabla_{\boldsymbol{x}} \Phi(\boldsymbol{x}, \boldsymbol{v}) + \mu_t(\boldsymbol{x})\Phi(\boldsymbol{x}, \boldsymbol{v}) &= S(\boldsymbol{x}, \boldsymbol{v}) + f(\boldsymbol{x}), \quad \text{in } \Omega \times \mathbb{S}^{d-1}, \\ \Phi(\boldsymbol{x}, \boldsymbol{v}) &= 0, \quad \text{on } \Gamma_-. \end{aligned} \tag{1.3}$$

In the rest of this paper, we focus on how to formulate an integral equation for the scattering term $S(\boldsymbol{x}, \boldsymbol{v})$ and how to solve it numerically.

For the isotropic scattering case, a Fredholm integral equation of the second kind of the mean local density can be directly obtained from the RTE [7,32]. We study the solvability of the integral equation based on the contraction principle and prove an a priori estimate of the solution. The numerical approach for solving the integral equation depends on whether the problem is spatially constant or not (i.e. whether the coefficients μ_t and μ_s independent on $\boldsymbol{x}$). For a homogeneous medium, the Fredholm kernel is simply a convolution, so the FFT can be used to evaluate the integral. Therefore, the Fredholm equation can be solved by combining the FFT with a standard iterative method such as MINRES [29] and GMRES [33]. For an inhomogeneous medium, we use the recursive skeletonization factorization (RSF) [21] method to factorize the dense linear system obtained from discretizing the integral equation. Due to the special factorization forms used in the RSF, this method is both fast and accurate.

For the anisotropic scattering case, noticing that the smooth anisotropic scattering term is a convolution on the unit sphere, we apply the Fourier transform ($d = 2$) and the spherical harmonic transform ($d = 3$) with respect to $\boldsymbol{v}$ to both σ and Φ. After truncating the expansion of σ due to its smoothness, we obtain a Fredholm integral equation of the second kind of the truncated expansion coefficients of Φ. Once solving this integral equation, one obtains the expansion coefficients of Φ in the angular variable $\boldsymbol{v}$ and thus the scattering term. Similar to the isotropic case, we study the solvability of the Fredholm equation by the contraction principle and proved an a priori estimate. Both the FFT-based method and the RSF-based method are discussed for the homogeneous and inhomogeneous cases, respectively. Numerical simulations are performed to demonstrate the efficiency of both the FFT-based method and the RSF-based method.

The rest of the paper is organized as follows. Section 2 addresses the isotropic scattering case, where we review the Fredholm integral equation of the mean local density, prove the uniqueness of the Fredholm equation, construct the FFT-based method and the RSF-based method, and report numerical studies. The anisotropic scattering case is studied in Section 3.

2. Isotropic scattering

This section studies the isotropic scattering case, i.e. $\sigma(\boldsymbol{x}, \boldsymbol{v} \cdot \boldsymbol{v}') \equiv 1$. We show the properties of the RTE, derive the Fredholm equation of the scattering term, construct the fast algorithms and report numerical studies.

2.1. Integral formulation

The integral formulation of the RTE has been studied in the literatures for example in [5,7,11,32]. Here for completeness, we provide a brief review of the integral equation of the RTE in the following, and refer readers to [7] for more details of the derivation.

Define the operators $\mathcal{T}$ and $\mathcal{A}$ as

$$\mathcal{T}\Psi := \boldsymbol{v}\cdot\nabla_{\boldsymbol{x}}\Psi + \mu_t\Psi, \quad \mathcal{A}\Psi(\boldsymbol{x}) := \fint_{\mathbb{S}^{d-1}} \Psi(\boldsymbol{x},\boldsymbol{v})\,\mathrm{d}\boldsymbol{v}, \tag{2.1}$$

then the RTE (1.1) can be reformulated as

$$\mathcal{T}\Phi - \mu_s\mathcal{A}\Phi = f. \tag{2.2}$$

By using the method of characteristics, we obtain

$$(\mathcal{T}^{-1}\Psi)(\boldsymbol{x},\boldsymbol{v}) = \int_0^{\tau(\boldsymbol{x},\boldsymbol{v})} \exp\left(-\int_0^s \mu_t\left(\boldsymbol{x}-s'\boldsymbol{v}\right)ds'\right)\Psi(\boldsymbol{x}-s\boldsymbol{v},\boldsymbol{v})\,\mathrm{d}s, \tag{2.3}$$

where $\tau(\boldsymbol{x},\boldsymbol{v})$ is the distance of a particle traveling from $\boldsymbol{x}$ to the domain boundary with the velocity $-\boldsymbol{v}$

$$\tau(\boldsymbol{x},\boldsymbol{v}) = \sup\{t : \boldsymbol{x}-s\boldsymbol{v}\in\Omega \text{ for } 0\le s<t\}. \tag{2.4}$$

Define the operator $\mathcal{J}:\Omega\to\Omega\times\mathbb{S}^{d-1}$ as $\mathcal{J}g(\boldsymbol{x},\boldsymbol{v}) = g(\boldsymbol{x})$ and introduce the mean local density as

$$u(\boldsymbol{x}) = \mathcal{A}\Phi(\boldsymbol{x}) = \fint_{\mathbb{S}^{d-1}} \Phi(\boldsymbol{x},\boldsymbol{v}')\,\mathrm{d}\boldsymbol{v}'. \tag{2.5}$$

The equation (2.2) can be reformulated as a Fredholm integral equation of the second kind with the form

$$u(\boldsymbol{x}) = \mathcal{K}u(\boldsymbol{x}) + \tilde{\mathcal{K}}f(\boldsymbol{x}), \tag{2.6}$$

where

$$\mathcal{K} = \mathcal{A}\mathcal{T}^{-1}\mathcal{J}\mu_s, \quad \tilde{\mathcal{K}} = \mathcal{A}\mathcal{T}^{-1}\mathcal{J}. \tag{2.7}$$

Notice that

$$\begin{aligned}(\tilde{\mathcal{K}}\phi)(\boldsymbol{x}) &= \fint_{\mathbb{S}^{d-1}}\int_0^{\tau(\boldsymbol{x},\boldsymbol{v})} \exp\left(-\int_0^s \mu_t\left(\boldsymbol{x}-s'\boldsymbol{v}\right)ds'\right)\phi(\boldsymbol{x}-s\boldsymbol{v})\,\mathrm{d}s\,\mathrm{d}\boldsymbol{v}\\ &= \frac{1}{|\mathbb{S}^{d-1}|}\int_\Omega \frac{1}{|\boldsymbol{x}-\boldsymbol{y}|^{d-1}}\exp\left(-|\boldsymbol{x}-\boldsymbol{y}|\int_0^1 \mu_t\left(\boldsymbol{x}-s'(\boldsymbol{x}-\boldsymbol{y})\right)ds'\right)\phi(\boldsymbol{y})\,\mathrm{d}\boldsymbol{y}.\end{aligned} \tag{2.8}$$

We have

$$(\tilde{\mathcal{K}}\phi)(\boldsymbol{x}) = \int_\Omega \tilde{K}(\boldsymbol{x},\boldsymbol{y})\phi(\boldsymbol{y})\,\mathrm{d}\boldsymbol{y}, \quad \tilde{K}(\boldsymbol{x},\boldsymbol{y}) = \frac{1}{|\mathbb{S}^{d-1}|}\frac{E(\boldsymbol{x},\boldsymbol{y})}{|\boldsymbol{x}-\boldsymbol{y}|^{d-1}}, \tag{2.9}$$

and

$$(\mathcal{K}\phi)(\boldsymbol{x}) = \int_\Omega K(\boldsymbol{x},\boldsymbol{y})\phi(\boldsymbol{y})\,\mathrm{d}\boldsymbol{y}, \quad K(\boldsymbol{x},\boldsymbol{y}) = \frac{\mu_s(\boldsymbol{y})}{|\mathbb{S}^{d-1}|}\frac{E(\boldsymbol{x},\boldsymbol{y})}{|\boldsymbol{x}-\boldsymbol{y}|^{d-1}}, \tag{2.10}$$

with $E(\boldsymbol{x},\boldsymbol{y}) = \exp\left(-|\boldsymbol{x}-\boldsymbol{y}|\int_0^1 \mu_t\left(\boldsymbol{x}-s'(\boldsymbol{x}-\boldsymbol{y})\right)ds'\right)$. Introducing $\tilde{u}(\boldsymbol{x}) = \mu_s(\boldsymbol{x})u(\boldsymbol{x})$ allows one to rewrite the integral equation (2.6) as

$$\tilde{u}(\boldsymbol{x}) = \mu_s(\boldsymbol{x})(\tilde{\mathcal{K}}\tilde{u})(\boldsymbol{x}) + \mu_s(\boldsymbol{x})(\tilde{\mathcal{K}}f)(\boldsymbol{x}), \tag{2.11}$$

or

$$\frac{\tilde{u}(\boldsymbol{x})}{\mu_s(\boldsymbol{x})} = (\tilde{\mathcal{K}}\tilde{u})(\boldsymbol{x}) + (\tilde{\mathcal{K}}f)(\boldsymbol{x}). \tag{2.11'}$$

The advantage of the formulation (2.11') is the symmetry of the kernel $\tilde{K}(\boldsymbol{x},\boldsymbol{y})$, i.e. $\tilde{K}(\boldsymbol{x},\boldsymbol{y}) = \tilde{K}(\boldsymbol{y},\boldsymbol{x})$, which can be used to save memory and calculation in numerical method.

2.2. Existence theory

The solvability of the RTE (1.1) was studied in the past decades [5,7,6,35,34,11]. Vladimirov in [38] studied the solvability of the integral equation using the compactness argument and the Riesz–Schauder theory but didn't provide an a priori estimate. Dautray and Lions in [7] developed a rather complete L^p theory for the RTE in the framework of semi-group theory. However, its a priori estimates for the solution are based on a rather strong assumption on μ_s and μ_t. In [35], Stefanov and Uhlmann studied the existence of solutions of RTE based on the compactness argument and the Fredholm theory. Based on the contraction principle, Egger and Schlottbom presented a L^p theory for RTE with relaxed conditions on the parameters μ_t, μ_s, and σ and also gave a sharp a priori estimate of the solution in [34,11,12]. The aim of this subsection is to translate the work of the RTE to the Fredholm equation case (2.6), study the properties of the operators $\mathcal{K}$ and $\tilde{\mathcal{K}}$ along with the solvability of the Fredholm equations (2.6), and present an a priori estimate of the solution. We start from the following assumptions:

(C1) $\Omega \in \mathbb{R}^d$ is a bounded Lipschitz domain;
(C2) $\mu_t, \mu_s : \Omega \to \mathbb{R}$ are non-negative and bounded on Ω, and $\mu_s(\boldsymbol{x}) \le \mu_t(\boldsymbol{x})$.

The main analytic result is the following theorem.

Theorem 1. *Under assumptions (C1) and (C2), for any $1 \le p \le \infty$ and $f \in L^p(\Omega)$, the Fredholm equation (2.6) admits a unique solution $u \in L^p(\Omega)$ which satisfies*

$$\|u\|_{L^p(\Omega)} \le \tau \exp\left(\tau \|\mu_s\|_{L^\infty(\Omega)}\right) \|f\|_{L^p(\Omega)}, \tag{2.12}$$

where $\tau = \sup_{\boldsymbol{x}\in\Omega, \boldsymbol{v}\in\mathbb{S}^{d-1}} \tau(\boldsymbol{x}, \boldsymbol{v})$.

The proof is divided into two cases: $p = \infty$ and $1 \le p < \infty$. For the case $p = \infty$, the following result holds.

Lemma 1. *Under assumptions (C1) and (C2), the linear operator $\mathcal{K} : L^\infty(\Omega) \to L^\infty(\Omega)$ is a contraction map with*

$$\|\mathcal{K}\|_{L^\infty(\Omega)\to L^\infty(\Omega)} \le C := 1 - \exp\left(-\tau \|\mu_s\|_{L^\infty(\Omega)}\right). \tag{2.13}$$

Assume $f \in L^\infty(\Omega)$, then

$$\left\|\tilde{\mathcal{K}} f\right\|_{L^\infty(\Omega)} \le \tau \|f\|_{L^\infty(\Omega)}. \tag{2.14}$$

Proof. Let $E^{[\mu_t]}(\boldsymbol{x}, \boldsymbol{v}, s) = \exp\left(-\int_0^s \mu_t(\boldsymbol{x} - s'\boldsymbol{v})\, \mathrm{d}s'\right)$, then

$$E^{[\mu_t]}(\boldsymbol{x} + s\boldsymbol{v}, \boldsymbol{v}, s) = E^{[\mu_t]}(\boldsymbol{x}, \boldsymbol{v}, s). \tag{2.15}$$

Recalling the definition of $\tilde{\mathcal{K}}$ (2.8), for $\phi(\boldsymbol{x}) \in L^\infty(\Omega)$, we have

$$|(\mathcal{K}\phi)(\boldsymbol{x})| = |(\tilde{\mathcal{K}}(\mu_s\phi))(\boldsymbol{x})| \le \|\phi\|_{L^\infty(\Omega)} |(\tilde{\mathcal{K}}\mu_s)(\boldsymbol{x})|.$$

Since $\mu_t(\boldsymbol{x}) \ge \mu_s(\boldsymbol{x})$ are bounded and non-negative, we obtain

$$\begin{aligned} 0 \le (\tilde{\mathcal{K}}\mu_s)(\boldsymbol{x}) &= \fint_{\mathbb{S}^{d-1}} \int_0^{\tau(\boldsymbol{x},\boldsymbol{v})} E^{[\mu_t]}(\boldsymbol{x}, \boldsymbol{v}, s)\mu_s(\boldsymbol{x} - s\boldsymbol{v})\, \mathrm{d}s\, \mathrm{d}\boldsymbol{v} \\ &\le \fint_{\mathbb{S}^{d-1}} \int_0^{\tau(\boldsymbol{x},\boldsymbol{v})} E^{[\mu_s]}(\boldsymbol{x}, \boldsymbol{v}, s)\mu_s(\boldsymbol{x} - s\boldsymbol{v})\, \mathrm{d}s\, \mathrm{d}\boldsymbol{v} \\ &\le \fint_{\mathbb{S}^{d-1}} \left(1 - \exp\left(-\|\mu_s\|_{L^\infty(\Omega)}\, \tau(\boldsymbol{x}, \boldsymbol{v})\right)\right) \mathrm{d}\boldsymbol{v} \le C < 1. \end{aligned} \tag{2.16}$$

Therefore $\|\mathcal{K}\phi(\boldsymbol{x})\|_{L^\infty(\Omega)} \le C\|\phi\|_{L^\infty(\Omega)} < \|\phi\|_{L^\infty(\Omega)}$ for any $\phi \in L^\infty(\Omega)$, i.e. $\mathcal{K}$ is a contraction map in $L^\infty(\Omega)$, and $\|\mathcal{K}\|_{L^\infty(\Omega)\to L^\infty(\Omega)} \le C$.

Recalling the definition of $\tilde{\mathcal{K}}$ (2.8), and noticing $0 < E^{[\mu_t]}(\boldsymbol{x}, \boldsymbol{v}, s) \le 1$, we have

$$|\tilde{\mathcal{K}} f| \le \left| \fint_{\mathbb{S}^{d-1}} \int_0^{\tau(\boldsymbol{x},\boldsymbol{v})} E^{[\mu_t]}(\boldsymbol{x}, \boldsymbol{v}, s)|f(\boldsymbol{x} - s\boldsymbol{v}')|\, \mathrm{d}s\, \mathrm{d}\boldsymbol{v} \right| \le \fint_{\mathbb{S}^{d-1}} \int_0^{\tau(\boldsymbol{x},\boldsymbol{v})} |f(\boldsymbol{x} - s\boldsymbol{v})|\, \mathrm{d}s\, \mathrm{d}\boldsymbol{v} \le \tau \|f\|_{L^\infty(\Omega)}. \quad \square$$

For the case $1 \le p < \infty$, notice that (2.6) can be rewritten as $u = \tilde{\mathcal{K}}(\mu_s u + f)$. By letting $w = \mu_s u + f$, the Fredholm equation (2.6) can be stated equivalently as

$$w = \mu_s \tilde{\mathcal{K}} w + f, \quad u = \tilde{\mathcal{K}} w. \tag{2.17}$$

Lemma 2. *Under assumptions (C1), (C2), the linear operator $\mu_s \tilde{\mathcal{K}} : L^p(\Omega) \to L^p(\Omega)$, $1 \le p < \infty$ is a contraction map with*

$$\left\| \mu_s \tilde{\mathcal{K}} \right\|_{L^p(\Omega) \to L^p(\Omega)} \le C, \tag{2.18}$$

and

$$\|u\|_{L^p(\Omega)} \le \tau \, \|w\|_{L^p(\Omega)} . \tag{2.19}$$

Proof. Recalling the definition of $\tilde{\mathcal{K}}$ (2.7), for any $\phi \in L^p(\Omega)$, we have

$$\begin{aligned}
\left\| \mu_s \tilde{\mathcal{K}} \phi \right\|_{L^p(\Omega)}^p &\le \int_\Omega \left(\mu_s(\boldsymbol{x}) \fint_{\mathbb{S}^{d-1}} \int_0^{\tau(\boldsymbol{x},\boldsymbol{v})} E^{[\mu_t]}(\boldsymbol{x}, \boldsymbol{v}, s) |\phi(\boldsymbol{x} - s\boldsymbol{v})| \, \mathrm{d}s \, \mathrm{d}\boldsymbol{v} \right)^p \mathrm{d}\boldsymbol{x} \\
&= \int_\Omega \left(\fint_{\mathbb{S}^{d-1}} \int_0^{\tau(\boldsymbol{x},\boldsymbol{v})} E^{[\mu_t]}(\boldsymbol{x}, \boldsymbol{v}, s) \mu_s(\boldsymbol{x} - s\boldsymbol{v}) \, \mathrm{d}s \, \mathrm{d}\boldsymbol{v} \right)^p |\phi(\boldsymbol{x})|^p \, \mathrm{d}\boldsymbol{x} \\
&\le C^p \, \|\phi\|_{L^p(\Omega)}^p < \|\phi\|_{L^p(\Omega)}^p ,
\end{aligned}$$

where the relation (2.15) and (2.16) are used in the equality and the last inequality, respectively. Therefore, $\mu_s \tilde{\mathcal{K}}$ is a contraction map in $L^p(\Omega)$ and $\left\| \mu_s \tilde{\mathcal{K}} \right\|_{L^p(\Omega) \to L^p(\Omega)} \le C$.

The non-negativeness of μ_t indicates $0 \le E^{[\mu_t]}(\boldsymbol{x}, \boldsymbol{v}, s) \le 1$, thus we have

$$\|u\|_{L^p(\Omega)}^p \le \int_\Omega \left(\fint_{\mathbb{S}^{d-1}} \int_0^{\tau(\boldsymbol{x},\boldsymbol{v})} E^{[\mu_t]}(\boldsymbol{x}, \boldsymbol{v}, s) |w(\boldsymbol{x} - s\boldsymbol{v})| \, \mathrm{d}s \, \mathrm{d}\boldsymbol{v} \right)^p \mathrm{d}\boldsymbol{x} \le \|\tau w\|_{L^p(\Omega)}^p . \quad \square$$

With these two lemmas, the proof of the Theorem 1 is rather straightforward.

Proof of Theorem 1. For the case $p = \infty$, noticing Lemma 1, and applying Banach's fixed point theorem [23, Chapter 3, Theorem 3.2], we obtain that (2.6) has a unique solution $u \in L^\infty(\Omega)$ if $\tilde{\mathcal{K}} f \in L^\infty(\Omega)$, which is guaranteed by (2.14).

Analogously, for the case $1 \le p < \infty$, noticing Lemma 2 and applying Banach's fixed point theorem, we obtain that (2.17) has a unique solution $w \in L^p(\Omega)$, which indicates (2.6) has a unique solution $u \in L^p(\Omega)$. The conclusion (2.12) is a directly deduction of Lemma 2. This completes the proof. $\square$

By setting $p = 2$ in Lemma 2, we can directly deduce the result.

Corollary 1. *Under assumptions (C1) and (C2), the linear operators $\mathcal{I} - \mathcal{K}$, $\mathcal{I} - \mu_s \tilde{\mathcal{K}}$: $L^2(\Omega) \to L^2(\Omega)$ are positive definite.*

Proof. Since $\mathcal{K} = \tilde{\mathcal{K}} \mu_s$, and $\tilde{\mathcal{K}}$ is a symmetric operator, for any $\phi \in L^2(\Omega)$, we have

$$\langle \phi, \mathcal{K} \phi \rangle = \langle \tilde{\mathcal{K}} \phi, \mu_s \phi \rangle = \langle \mu_s \tilde{\mathcal{K}} \phi, \phi \rangle.$$

Using (2.18) with $p = 2$ and Hölder inequality, we can obtain

$$\left\langle \left(\mathcal{I} - \mu_s \tilde{\mathcal{K}} \right) \phi, \phi \right\rangle \ge (1 - C) \, \|\phi\|_{L^2(\Omega)}^2 .$$

Since $C < 1$, $\mathcal{I} - \mathcal{K}$ and $\mathcal{I} - \mu_s \tilde{\mathcal{K}}$ are both positive definite. $\square$

2.3. Fast algorithms

In this subsection, we assume that μ_s has a positive lower bound and study the fast algorithms for solving (2.11'). These algorithms can also be applied to (2.6). Solving (2.11) requires two steps:

S.1 Evaluate $(\tilde{\mathcal{K}} f)(\boldsymbol{x})$;

S.2 Given $r(\boldsymbol{x})$, solve $\left(\frac{\mathcal{I}}{\mu_s(\boldsymbol{x})} - \tilde{\mathcal{K}}\right)\tilde{u}(\boldsymbol{x}) = r(\boldsymbol{x})$, or equivalently $\tilde{u}(\boldsymbol{x}) = \left(\frac{\mathcal{I}}{\mu_s(\boldsymbol{x})} - \tilde{\mathcal{K}}\right)^{-1} r(\boldsymbol{x})$.

To simplify the discussion, we assume that the domain Ω is rectangular. The discretization of the Fredholm equation (2.11') starts by partitioning the domain Ω into Cartesian cells of equal volume. Let N be the number of the cells and $\{\boldsymbol{x}_i\}_{1\le i\le N}$ be the center of the cells. We introduce $\tilde{u}_i$ as an approximation of $\tilde{u}(\boldsymbol{x}_i)$ and define $\mu_{s,i} = \mu_s(\boldsymbol{x}_i)$ and $f_i = f(\boldsymbol{x}_i)$. Using the Nyström method, the discretization of (2.11') takes the following form

$$\frac{\tilde{u}_i}{\mu_{s,i}} = \sum_{j=1}^{N} \tilde{K}_{i,j}\tilde{u}_j + \sum_{j=1}^{N} \tilde{K}_{i,j} f_j. \tag{2.20}$$

When $i \neq j$, $\tilde{K}_{i,j}$ is equal to $\tilde{K}(\boldsymbol{x}_i, \boldsymbol{x}_j)$ scaled by the cell volume. When $i = j$ since $\tilde{K}(\boldsymbol{x}, \boldsymbol{y})$ is singular at $\boldsymbol{x} = \boldsymbol{y}$, the value $\tilde{K}_{i,i}$ is taken to be the integral of $\tilde{K}$ at the i-th cell. We remark that the spatial discretization is usually problem depended, and here we don't pay much attention on it. One can extend the following algorithms to other the spatial discretization straightly.

Setting $\tilde{\mathbf{K}} = \left(\tilde{K}_{ij}\right)_{N\times N}$ and $\mathbf{A} = \left(\frac{\delta_{ij}}{\mu_{s,i}} - \tilde{K}_{ij}\right)_{N\times N}$ allows one to rewrite (2.20) in the following matrix form

$$\mathbf{A}\tilde{\boldsymbol{u}} = \tilde{\mathbf{K}}\boldsymbol{f}, \tag{2.21}$$

where $\tilde{\boldsymbol{u}} = \left(\tilde{u}_i\right)$ and $\boldsymbol{f} = (f_i)$. Corollary 1 guarantees the matrix $\mathbf{A}$ is positive definite. Finally, in order to get the approximation $\boldsymbol{u} = (u_i)$ for the values of $u(\boldsymbol{x})$ at $\boldsymbol{x}_i$, we simply set $u_i = \tilde{u}_i/\mu_{s,i}$.

In the calculation of $\tilde{K}_{ij}$, there is a line integral in $E(\boldsymbol{x}_i, \boldsymbol{x}_j)$. The approach of [32] uses the Fourier transform of μ_t to evaluate the integral. The computational cost is proportional to the number of the Fourier modes used in the integral. Even μ_t is quite smooth, this method can be somewhat inefficient in practice. Here we use the Gauss–Legendre quadrature for the line integral. In all tests of this paper, the Gauss–Legendre quadrature with merely 5 points give sufficiently accurate results for smooth μ_t.

The calculation of $\tilde{K}_{ii}$ requires evaluating an integral of a singular function in a grid cell. Noticing that $\tilde{K}(\boldsymbol{x}, \boldsymbol{y}) = \frac{1}{|\mathbb{S}^{d-1}||\boldsymbol{x}-\boldsymbol{y}|^{d-1}} + \frac{1}{|\mathbb{S}^{d-1}|}\frac{E(\boldsymbol{x},\boldsymbol{y})-1}{|\boldsymbol{x}-\boldsymbol{y}|^{d-1}}$, we first evaluate the mean of the first part by analysis and then apply the Gauss–Legendre quadrature for the second part. We note that the second part is not smooth in the whole cell because of the $|\cdot|$. In practice, we split the cell into 2^d quadrants and apply the numerical quadrature in each quadrants. Numerical test shows the Gauss–Legendre quadrature with 15 points gives accurate results.

To solve (2.21), a typical direct method proceeds by constructing $\mathbf{A}$, factorizing it with either LU or Cholesky decomposition, and solving it with backward/forward substitution. The computational cost of such a direct method scales like $O(N^3)$, where N is the number of discrete points of Ω. This is rather costly where N is large and in what follows we study fast alternatives.

2.3.1. Homogeneous media and FFT-based algorithm

For a homogeneous medium, the total transport coefficient μ_t is independent on $\boldsymbol{x}$. The kernel

$$\tilde{K}(\boldsymbol{x}, \boldsymbol{y}) = \frac{1}{|\mathbb{S}^{d-1}|}\frac{\exp\left(-\mu_t|\boldsymbol{x}-\boldsymbol{y}|\right)}{|\boldsymbol{x}-\boldsymbol{y}|^{d-1}} := \kappa(\boldsymbol{x}-\boldsymbol{y}) \tag{2.22}$$

only depends on $|\boldsymbol{x}-\boldsymbol{y}|$ and this indicates that $\tilde{\mathcal{K}} f(\boldsymbol{x})$ is a convolution. If the domain Ω is a rectangle ($d = 2$) or cuboid ($d = 3$), the Fourier transformation can be used to calculate the convolution more efficiently. More precisely, let us assume $\Omega = [0,1]^d$ and then $\kappa(\boldsymbol{x})$ is defined on $[-1,1]^d$. One then extends $\kappa(\boldsymbol{x})$ periodically to the whole space and redefines $\tilde{K}(\boldsymbol{x}, \boldsymbol{y}) = \kappa(\boldsymbol{x}-\boldsymbol{y})$, $\boldsymbol{x}, \boldsymbol{y} \in \mathbb{R}^d$. For any function $\phi(\boldsymbol{x})$, $\boldsymbol{x} \in [0,1]^d$, extending it to $[-1,1]^d$ by padding zero (and still denoting it by ϕ), we obtain

$$\tilde{\mathcal{K}}\phi(\boldsymbol{x}) = \int_{[-1,1]^d} \kappa(\boldsymbol{x}-\boldsymbol{y})\phi(\boldsymbol{y})\,\mathrm{d}\boldsymbol{y}, \tag{2.23}$$

which can be evaluated by the Fourier transformation. If the discretization in (2.20) is uniform, then the matrix $\tilde{\mathbf{K}} = (\tilde{K}_{i,j})_{N\times N}$ is a circulant matrix, thus the FFT can be employed to evaluate $\tilde{\mathbf{K}}\tilde{\boldsymbol{u}}$ and $\tilde{\mathbf{K}}\boldsymbol{f}$, with the computation cost reduced to $O(N\log(N))$ with $N = n^d$. Hence, the application of the operators $\tilde{\mathcal{K}}$ and $\frac{\mathcal{I}}{\mu_s(\boldsymbol{x})} - \tilde{\mathcal{K}}$ is highly efficient and Step S.2 can be evaluated by a standard iterative method, for example MINRES [29] and GMRES [33].

Before the evaluation of $\tilde{\mathcal{K}}\phi(\boldsymbol{x})$, one needs to calculate the Fourier modes of $\kappa(\boldsymbol{x})$, which costs $O(N\log(N))$ computation steps and $O(N)$ storage. Therefore, the precomputing cost of the algorithm is $O(N\log(N))$. The computation cost of the two steps S.1 and S.2 are $O(N\log(N))$ and $O(n_{iter}N\log(N))$, respectively, where n_{iter} the number of iterations used in the iterative method. As a result, the total computation cost is $O(n_{iter}N\log(N))$.

Remark 1. The algorithm presented in this subsection can be applied to (2.6) without any difficulty. The differences are that we also have to assume μ_s is independent on $\boldsymbol{x}$, and in solving Step S.2, the iterative method including MINRES does not work because the kernel $K(\boldsymbol{x},\boldsymbol{y})$ is not symmetric.

2.3.2. Inhomogeneous media and RSF-based algorithm

The FFT-based algorithm in Section 2.3.1 has a strong requirement that the total transport coefficient μ_t is constant. Moreover, Step S.2 dominates the computation cost of the whole algorithm. When the number of iterations is large or there are multiple right hand sides, the iterative methods can be somewhat inefficient. The fast multipole based algorithm in [32] shares the same issue since an iterative method is also used in Step S.2.

The recently proposed *recursive skeletonization factorization* (RSF) in [22] provides an alternative. Building on top of earlier work in [17,20], the RSF constructs a multiplicative factorization of the matrix operator using a sparsification technique called *interpolative decomposition* recursively. This representation enables surprisingly simple algorithms to apply $\mathbf{A}$ and $\mathbf{A}^{-1}$ directly. This makes it rather easy to solve (2.21). RSF is based on elimination, so it requires certain intermediate matrices to be invertible, which is guaranteed by Corollary 1. For more details of RSF, we refer the readers to [22, Section 3].

When the matrix $\mathbf{A}$ is factorized recursively, the RSF takes advantage of the low-rank behavior of the off-diagonal entries of the matrix and thus avoids visiting all entries of $\mathbf{A}$. More precisely from [22], for a Fredholm integral equation of the second kind, the RSF only visits $O(N\log(N))$ entries of $\mathbf{A}$. The cost t_f of factorizing $\mathbf{A}$ and the cost $t_{a/s}$ of evaluating $\mathbf{A}\boldsymbol{f}$ as well as $\mathbf{A}^{-1}\boldsymbol{f}$ are respectively given by

$$t_f = \begin{cases} O(N^{3/2}), & d=2 \\ O(N^2), & d=3, \end{cases} \qquad t_{a/s} = \begin{cases} O(N\log N), & d=2, \\ O(N^{4/3}), & d=3. \end{cases} \tag{2.24}$$

Thus, the precomputation cost of the algorithm is t_f, and the costs of Steps S.1 and S.2 are both $t_{a/s}$, with no iterations involved.

As we pointed out, the FFT-based algorithm has strong requirements on the total transport coefficient μ_t (i.e., constant) and the domain Ω, while the RSF-based works for any μ_t and domain Ω. However, even for the case of constant μ_t, sometimes it is preferred to use the RSF-based algorithm. The nice feature of the RSF-based algorithm is that, for any additional right hand side, the extra cost is merely $t_{a/s}$. Therefore, when one needs to solve (2.11) for many different source terms f, the RSF-based algorithm shows its advantage.

Remark 2. Since the kernel $\tilde{K}(\boldsymbol{x},\boldsymbol{y})$ is symmetric, the matrix $\tilde{\mathbf{A}}$ is symmetric as well. RSF will use this property to save storage memory and factorization time (save nearly half memory and time [21]). The RSF-based algorithm can be directly applied on (2.6). However, due to the lack of symmetry in the kernel $K(\boldsymbol{x},\boldsymbol{y})$, RSF has to factorize a non-symmetric matrix with extra computational and storage costs.

2.4. Numerical results

Here we provide several numerical examples to study the complexity and accuracy of the direct method, the FFT-based method and the RSF-based method. The computational cost consists of two parts: the precomputation part and the solution part, denoted by T_{pre} and T_{sol}, respectively. The precomputation part is the time used for preparing and inverting $\mathbf{A}$ for the direct method; preparing the convolution vector for the FFT-based method; or factorizing $\mathbf{A}$ for the RSF-based method.

The solution part is the time used for solving a single linear system (2.21), i.e., applying $\mathbf{A}^{-1}$ for the direct method; applying GMRES/MINRES for the FFT-based method; or applying the factorized inverse $\mathbf{A}^{-1}$ for the RSF-based method. Here, we will use the superscripts DIR, FFT and RSF to denote the corresponding quantities for these three methods, respectively. For example, $T_{\text{pre}}^{\text{RSF}}$ denotes the precomputation time of the RSF-based method. All the numerical simulations are performed in MATLAB R2016b on a single core (without parallelization) of an Intel(R) Xeon(R) CPU E5-1620 0 @ 3.60 GHz on a 64-bit Linux desktop with 32 GB of RAM.

The parameter ϵ is used to control the designed accuracy of the solution. In the FFT-based method ϵ is the desired tolerance of the GMRES/MINRES method, while in the RSF-based method ϵ is the relative accuracy parameter of the RSF. To measure the accuracy, we introduce the relative L^2 error

$$\mathcal{E} = \frac{\|\boldsymbol{u}-\boldsymbol{u}_{\text{ref}}\|_{L^2}}{\|\boldsymbol{u}_{\text{ref}}\|_{L^2}}, \tag{2.25}$$

where $\boldsymbol{u}$ is the solution obtained either from the FFT-based or from the RSF-based method and $\boldsymbol{u}_{\text{ref}}$ is the reference solution. Similar to the computational cost, we use the superscripts FFT and RSF to denote the relative error of these two methods, respectively.

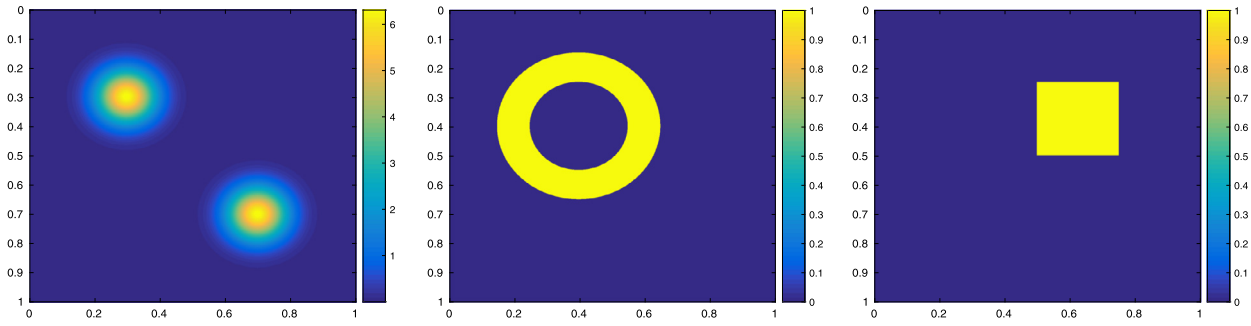

(a) f_1 in (2.26a) (b) f_2 in (2.26b) (c) f_3 in (2.26c)

Fig. 1. Source terms (2.26) used in numerical simulation. (For interpretation of the colors in the figure(s), the reader is referred to the web version of this article.)

Table 1
Isotropic scattering case: computational cost of three methods for different n and ϵ with constant scattering coefficient $\mu_s = 1$ and transport coefficient $\mu_t = 1.2$.

n	ϵ	$T_{\text{pre}}^{\text{DIR}}$ (sec)	$T_{\text{pre}}^{\text{FFT}}$ (sec)	$T_{\text{pre}}^{\text{RSF}}$ (sec)	$T_{\text{sol}}^{\text{DIR}}$ (sec)	$T_{\text{sol}}^{\text{FFT}}$ (sec)	$T_{\text{sol}}^{\text{RSF}}$ (sec)
32	$1E{-}4$	$3.39E{-}2$	$3.23E{-}4$	$5.75E{-}2$	$1.86E{-}3$	$2.99E{-}3$	$2.53E{-}3$
64	$1E{-}4$	$9.19E{-}1$	$9.45E{-}4$	$4.34E{-}1$	$2.44E{-}2$	$9.32E{-}3$	$1.27E{-}2$
128	$1E{-}4$	$5.04E{+}1$	$1.76E{-}3$	$3.32E{+}0$	$3.78E{-}1$	$1.52E{-}2$	$6.91E{-}2$
256	$1E{-}4$	–	$8.65E{-}3$	$2.36E{+}1$	–	$9.71E{-}2$	$3.51E{-}1$
512	$1E{-}4$	–	$3.97E{-}2$	$1.93E{+}2$	–	$2.83E{-}1$	$1.78E{+}0$
32	$1E{-}6$	$3.39E{-}2$	$3.23E{-}4$	$8.08E{-}2$	$1.86E{-}3$	$3.16E{-}3$	$2.67E{-}3$
64	$1E{-}6$	$9.19E{-}1$	$9.45E{-}4$	$7.24E{-}1$	$2.44E{-}2$	$1.02E{-}2$	$1.38E{-}2$
128	$1E{-}6$	$5.04E{+}1$	$1.76E{-}3$	$6.12E{+}0$	$3.78E{-}1$	$1.74E{-}2$	$8.05E{-}2$
256	$1E{-}6$	–	$8.65E{-}3$	$4.43E{+}1$	–	$9.52E{-}2$	$4.41E{-}1$
512	$1E{-}6$	–	$3.97E{-}2$	$3.87E{+}2$	–	$3.33E{-}1$	$2.21E{+}0$
32	$1E{-}8$	$3.39E{-}2$	$3.23E{-}4$	$9.63E{-}2$	$1.86E{-}3$	$3.18E{-}3$	$2.79E{-}3$
64	$1E{-}8$	$1.01E{+}0$	$9.45E{-}4$	$9.79E{+}0$	$2.44E{-}2$	$1.20E{-}2$	$1.42E{-}2$
128	$1E{-}8$	$5.04E{+}1$	$1.76E{-}3$	$1.00E{+}1$	$3.78E{-}1$	$2.20E{-}2$	$1.05E{-}1$
256	$1E{-}8$	–	$8.65E{-}3$	$8.96E{+}1$	–	$1.47E{-}1$	$6.64E{-}1$
512	$1E{-}8$	–	$3.97E{-}2$	$7.84E{+}2$	–	$3.60E{-}1$	$3.74E{+}0$

Three source terms used in the simulations are

$$f_1(\boldsymbol{x}) = \frac{1}{\sqrt{2\pi T}} \exp\left(-\frac{|\boldsymbol{x}-\boldsymbol{c}_1|^2}{2T}\right) + \frac{1}{\sqrt{2\pi T}} \exp\left(-\frac{|\boldsymbol{x}-\boldsymbol{c}_2|^2}{2T}\right), \tag{2.26a}$$

$$f_2(\boldsymbol{x}) = \begin{cases} 1 & \text{if } |\boldsymbol{x}-\boldsymbol{c}_3| \in [3/20, 1/4], \\ 0 & \text{otherwise}, \end{cases} \tag{2.26b}$$

$$f_3(\boldsymbol{x}) = \begin{cases} 1, & \text{if } x_1, x_2 \in [1/2, 3/4], \\ 0, & \text{otherwise}, \end{cases} \tag{2.26c}$$

with $T = 4E{-}3, \boldsymbol{c}_1 = (3/10, 7/10), \boldsymbol{c}_2 = (7/10, 3/10), \boldsymbol{c}_3 = (3/5, 2/5)$. Fig. 1 plots the contour of these source terms. The computational domain Ω is chosen as the unit square, i.e. $\Omega = [0,1]^2$. The domain is uniformly discretized by n points in each direction.

These numerical examples test for different n, different tolerance ϵ, and different scattering coefficients μ_s and μ_t. Because the FFT-based method only works for the constant transport coefficient case, we report the constant transport coefficient case and the variable coefficient case separately.

2.4.1. Homogeneous media

Computational cost We perform simulation for different mesh sizes $n = 32$, 64, 128, 256 and 512 and different tolerance ϵ as $1E{-}4$, $1E{-}6$ and $1E{-}8$, and for the constant scattering coefficient $\mu_s = 1$ and $\mu_t = 1.2$ to study the computational cost of three methods. The results are summarized in Table 1. The source term is given in (2.26a). The FFT-based method is the fastest in both precomputation and solution. Comparing the solution time, one finds that the RSF-based method is only a little slower than the FFT-based method. Both the RSF-based method and direct method need to decompose the matrix, but the RSF is faster in both precomputation and solution steps.

For a fixed mesh size n, when ϵ changes, the solution time of the FFT-based method changes as well because ϵ affects the number of iterative steps of MINRES. Both the precomputation time and the solution time of the RSF-based method

Table 2
Isotropic scattering case: relative error of the FFT-based method and RSF-based method for three source term in (2.26) with constant scattering coefficient $\mu_s = 1$ and transport coefficient $\mu_t = 1.2$. $\mathcal{E}_k$ is the relative error for the source term f_k, $k = 1, 2, 3$.

n	ϵ	$\mathcal{E}_1^{\text{FFT}}$	$\mathcal{E}_1^{\text{RSF}}$	$\mathcal{E}_2^{\text{FFT}}$	$\mathcal{E}_2^{\text{RSF}}$	$\mathcal{E}_3^{\text{FFT}}$	$\mathcal{E}_3^{\text{RSF}}$
32	1E−4	2.66E−6	1.81E−5	1.44E−5	1.85E−5	2.10E−5	1.65E−5
64	1E−4	2.69E−6	2.67E−5	1.44E−5	2.49E−5	2.10E−5	2.23E−5
128	1E−4	2.70E−6	1.96E−5	1.43E−5	1.88E−5	7.69E−7	1.69E−5
256	1E−4	2.71E−6	1.89E−5	3.81E−7	1.74E−5	7.70E−7	1.49E−5
512	1E−4	2.72E−6	1.69E−5	3.82E−7	1.49E−5	7.71E−7	1.34E−5
32	1E−6	8.96E−8	2.74E−7	3.72E−7	2.77E−7	7.49E−7	2.50E−7
64	1E−6	9.01E−8	3.06E−7	1.64E−8	3.04E−7	2.47E−8	2.68E−7
128	1E−6	9.04E−8	4.60E−7	1.64E−8	4.64E−7	2.49E−8	4.17E−7
256	1E−6	9.07E−8	4.37E−7	1.64E−8	4.23E−7	2.49E−8	3.73E−7
512	1E−6	3.12E−9	4.61E−7	1.64E−8	4.49E−7	2.49E−8	4.00E−7
32	1E−8	3.02E−9	3.16E−9	6.06E−10	3.01E−9	1.03E−9	2.62E−9
64	1E−8	3.07E−9	1.25E−8	7.01E−10	1.30E−8	1.18E−9	1.19E−8
128	1E−8	5.09E−11	1.92E−8	7.07E−10	1.94E−8	1.20E−9	1.77E−8
256	1E−8	5.12E−11	1.73E−8	7.07E−10	1.70E−8	4.13E−11	1.53E−8
512	1E−8	5.14E−11	2.04E−8	2.63E−11	2.04E−8	4.13E−11	1.86E−8

Table 3
Isotropic scattering case: computational cost and relative error for different scattering coefficient μ_s and ϵ with $n = 128$ and $\mu_t = \mu_s + 0.2$.

μ_s	ϵ	$T_{\text{pre}}^{\text{FFT}}$	$T_{\text{pre}}^{\text{RSF}}$	$T_{\text{sol}}^{\text{FFT}}$	$T_{\text{sol}}^{\text{RSF}}$	$\mathcal{E}^{\text{FFT}}$	$\mathcal{E}^{\text{RSF}}$
1	1E−4	1.82E−3	3.01E+0	1.51E−2	6.84E−2	2.70E−6	2.34E−5
10	1E−4	1.82E−3	3.05E+0	3.42E−2	7.05E−2	1.82E−6	5.59E−4
100	1E−4	1.82E−3	2.79E+0	4.53E−2	7.02E−2	1.85E−5	9.06E−5
1	1E−6	1.76E−3	5.16E+0	1.92E−2	8.18E−2	9.04E−8	4.83E−7
10	1E−6	1.78E−3	5.28E+0	4.16E−2	9.73E−2	3.81E−8	2.20E−6
100	1E−6	1.80E−3	4.24E+0	6.84E−2	9.34E−2	1.18E−7	1.77E−6
1	1E−8	1.78E−3	9.06E+0	2.29E−2	1.11E−1	5.09E−11	1.81E−8
10	1E−8	1.74E−3	9.71E+0	3.74E−2	1.18E−1	9.82E−11	9.44E−9
100	1E−8	1.75E−3	8.13E+0	8.83E−2	1.04E−1	1.36E−9	3.75E−9

are affected as well. When ϵ decreases, more skeletonization points are selected in the RSF, so both the precomputation and solution time increase. It is worth to point out that even for $\epsilon = 1E-8$, the computational cost of RSF-based method is smaller than the direct method if $n \geq 64$. When $n \geq 256$, due to the limitation of RAM, the direct method fails to work any more.

Comparing these three methods, one observes that the FFT-based method is the fastest one for the constant case. The solution time of RSF-based method is comparable with the FFT-based method and its precomputation time is faster than the direct method if n is not small.

Relative error Simulations for different mesh size n and different tolerance ϵ are performed to study the relative error. Table 2 presents the relative error of the FFT-based method and the RSF-based method for the three source terms (2.26) with $\mu_s = 1$ and $\mu_t = 1.2$. The reference solution is the solution of the direct method if $n = 32$, 64 and 128. For $n > 128$, the reference solution is computed with the FFT-based method with a very small relative tolerance for MINRES. Both the two methods behavior well on the relative error.

Behavior for different scattering coefficients Here we study the dependence on the scattering coefficient μ_s for the source term (2.26a). When μ_s is small, for example $\mu_s = 1$, the physics corresponds to the transport regime for the photon. The case of relatively large μ_s, for example $\mu_s = 100$, corresponds to the diffusive regime. Here we always set $\mu_t = \mu_s + 0.2$. The simulation results for $\mu_s = 1, 10, 100$ are listed in Table 3. Because the use of MINRES, for different μ_s, the solution time of the FFT-based method varies significantly as the iterations are quite different. The RSF-based method is quite robust in terms of the scattering coefficient. This indicates that these two methods work in both diffusive regimes and transport regimes, and the RSF-based method is quite insensitive to the parameters.

2.4.2. Inhomogeneous media

When the transport coefficient μ_t depends on $\boldsymbol{x}$, the FFT-based method fails to work. Here we test the RSF-based method for the variable transport coefficient case. The scattering coefficient takes the form of

Table 4
Isotropic scattering case: computational cost of the direct method and RSF-based method for different n and ϵ with variable scattering coefficient (2.27) with $\rho = 1$ and $\mu_t = \mu_s + 0.2$.

n	ϵ	$T_{\text{pre}}^{\text{DIR}}$ (sec)	$T_{\text{pre}}^{\text{RSF}}$ (sec)	$T_{\text{sol}}^{\text{DIR}}$ (sec)	$T_{\text{sol}}^{\text{RSF}}$ (sec)
32	$1E{-4}$	$1.62E{-1}$	$1.41E{-1}$	$2.51E{-3}$	$3.22E{-3}$
64	$1E{-4}$	$1.94E{+0}$	$7.16E{-1}$	$2.32E{-2}$	$1.33E{-2}$
128	$1E{-4}$	$6.84E{+1}$	$5.01E{+0}$	$4.13E{-1}$	$6.72E{-2}$
256	$1E{-4}$	–	$3.81E{+1}$	–	$3.56E{-1}$
512	$1E{-4}$	–	$2.81E{+2}$	–	$1.77E{+0}$
32	$1E{-6}$	$1.62E{-1}$	$1.67E{-1}$	$2.51E{-3}$	$3.85E{-3}$
64	$1E{-6}$	$1.94E{+0}$	$1.05E{+0}$	$2.32E{-2}$	$1.40E{-2}$
128	$1E{-6}$	$6.84E{+1}$	$8.66E{+0}$	$4.13E{-1}$	$7.84E{-2}$
256	$1E{-6}$	–	$6.72E{+1}$	–	$4.35E{-1}$
512	$1E{-6}$	–	$5.20E{+2}$	–	$2.26E{+0}$
32	$1E{-8}$	$1.62E{-1}$	$1.84E{-1}$	$2.51E{-3}$	$4.07E{-3}$
64	$1E{-8}$	$1.94E{+0}$	$1.43E{+0}$	$2.32E{-2}$	$1.46E{-2}$
128	$1E{-8}$	$6.84E{+1}$	$1.35E{+1}$	$4.13E{-1}$	$1.12E{-1}$
256	$1E{-8}$	–	$1.19E{+2}$	–	$6.15E{-1}$
512	$1E{-8}$	–	$9.59E{+2}$	–	$3.40E{+0}$

Table 5
Isotropic scattering case: relative error of the RSF-based method for three source terms (2.26) with variable scattering term (2.27) with $\rho = 1$ and $\mu_t = \mu_s + 0.2$. $\mathcal{E}_k$ is the relative error for the source term f_k.

n	ϵ	$\mathcal{E}_1^{\text{RSF}}$	$\mathcal{E}_2^{\text{RSF}}$	$\mathcal{E}_3^{\text{RSF}}$
32	$1E{-4}$	$2.02E{-5}$	$2.02E{-5}$	$1.70E{-5}$
64	$1E{-4}$	$4.19E{-5}$	$3.03E{-5}$	$2.31E{-5}$
128	$1E{-4}$	$3.04E{-5}$	$2.32E{-5}$	$2.05E{-5}$
32	$1E{-6}$	$3.05E{-7}$	$3.36E{-7}$	$3.05E{-7}$
64	$1E{-6}$	$2.88E{-7}$	$3.11E{-7}$	$2.35E{-7}$
128	$1E{-6}$	$4.29E{-7}$	$4.43E{-7}$	$3.51E{-7}$
32	$1E{-8}$	$6.49E{-9}$	$8.73E{-9}$	$6.50E{-9}$
64	$1E{-8}$	$6.43E{-9}$	$6.71E{-9}$	$6.01E{-9}$
128	$1E{-8}$	$1.33E{-8}$	$1.42E{-8}$	$1.06E{-8}$

$$\mu_s(\boldsymbol{x}) = 1 + \rho \exp\left(-\frac{|\boldsymbol{x} - \boldsymbol{c}|^2}{4}\right), \quad \boldsymbol{c} = \left(\frac{1}{2}, \frac{1}{2}\right), \tag{2.27}$$

where ρ is constant.

Computational cost We perform the simulations for different mesh size n and different tolerance ϵ for the scattering term (2.27) with $\rho = 1$. The computational costs of the direct method and the RSF-based method are presented in Table 4. The source term is chosen to be (2.26a). Since μ_t depends on $\boldsymbol{x}$, one has to calculate a line integral in the evaluation of each entry of the matrix $\mathbf{A}$. However, because the factorization dominates the computational cost for the two methods, the precomputation time is only a bit slower than the constant scattering case.

Comparing these two methods, when $n \geq 64$, the RSF-based method becomes faster than the direct method in both the precomputation and solution parts.

Relative error Table 5 presents the relative error for different mesh size n and different tolerance ϵ with the scattering term (2.27) with $\rho = 1$ and $\mu_t = \mu_s + 0.2$. The reference solution is calculated by the direct method and the relative error behaves similarly as in the constant scattering case.

Behavior for different scattering coefficients Here we study the dependence of the computational cost and accuracy of the methods on the scattering coefficient μ_s for the source term (2.26a). As before, $\mu_t = \mu_s + 0.2$. The simulation results for $\rho = 1, 10, 100$ in (2.27) are listed in Table 6. Similar as in the constant transport coefficient case, the RSF-based method is quite robust in terms of the scattering coefficient. This indicates that the RSF-based method works well in both diffusive regimes and transport regimes and is insensitive to different regimes.

Table 6
Isotropic scattering case: computational cost and relative error for different ρ in (2.27) and ϵ with $n = 128$ and $\mu_t = \mu_s + 0.2$.

ρ	ϵ	$T_{\text{pre}}^{\text{RSF}}$	$T_{\text{sol}}^{\text{RSF}}$	$\mathcal{E}^{\text{RSF}}$
1	1E−4	4.91E+0	7.02E−2	2.97E−5
10	1E−4	4.97E+0	7.23E−2	2.42E−4
100	1E−4	4.56E+0	7.08E−2	1.47E−4
1	1E−6	9.41E+0	7.91E−2	4.47E−7
10	1E−6	9.44E+0	8.38E−2	3.03E−6
100	1E−6	6.91E+0	9.43E−2	7.52E−7
1	1E−8	1.31E+1	1.19E−1	1.49E−8
10	1E−8	1.39E+1	1.17E−1	8.52E−9
100	1E−8	1.08E+1	9.89E−2	3.04E−9

3. Anisotropic scattering

This section studies the RTE with anisotropic scattering. The start point is the observation that the scattering term $\mu_s(\boldsymbol{x}) \fint_{\mathbb{S}^{d-1}} \sigma(\boldsymbol{x}, \boldsymbol{v}\cdot\boldsymbol{v}')\Phi(\boldsymbol{x}, \boldsymbol{v}')\,\mathrm{d}\boldsymbol{v}'$ is a convolution on sphere. Thus the Fourier transformation for $d = 2$ and the spherical harmonic transformation for $d = 3$ can be used to simplify the scattering term.

3.1. Integral formulation

The RTE (1.1) has been well studied in [5,7,14,34,11]. Here, we extend the derivation in Section 2.1 to the anisotropic case. The extension is not trivial due to the complexity of the scattering term.

For the anisotropic case, let us redefine the operator $\mathcal{A}$ as

$$(\mathcal{A}\Psi)(\boldsymbol{x}, \boldsymbol{v}) := \fint_{\mathbb{S}^{d-1}} \sigma(\boldsymbol{x}, \boldsymbol{v}\cdot\boldsymbol{v}')\Psi(\boldsymbol{x}, \boldsymbol{v}')\,\mathrm{d}\boldsymbol{v}', \tag{3.1}$$

then the RTE (1.1) can be solved as

$$\Phi(\boldsymbol{x}, \boldsymbol{v}) = \mathcal{T}^{-1}\mu_s\mathcal{A}\Phi + \mathcal{T}^{-1}\mathcal{J}f, \tag{3.2}$$

where $\mathcal{T}^{-1}$ and $\mathcal{J}$ are same as those in Section 2.

Notice $(\mathcal{A}\Phi)(\boldsymbol{x}, \boldsymbol{v}) := \fint_{\mathbb{S}^{d-1}} \sigma(\boldsymbol{x}, \boldsymbol{v}\cdot\boldsymbol{v}')\Phi(\boldsymbol{x}, \boldsymbol{v}')\,\mathrm{d}\boldsymbol{v}'$ is a convolution on sphere. Since the formulas for $2D$ and $3D$ are quite different, we discuss them separately.

3.1.1. 2D case

In 2D ($d = 2$), $\boldsymbol{v} = (\cos(\theta), \sin(\theta))$. The operator $\mathcal{A}$ can be rewritten as

$$(\mathcal{A}\Phi)(\boldsymbol{x}, \theta) = \fint_0^{2\pi} \sigma(\boldsymbol{x}, \theta - \theta')\Phi(\boldsymbol{x}, \theta')\,\mathrm{d}\theta'. \tag{3.3}$$

Applying Fourier transformation on Φ and σ with respect to θ on $[0, 2\pi]$ gives rise to

$$(\mathcal{A}\Phi)(\boldsymbol{x}, \theta) = \sum_{k=-\infty}^{\infty} \hat{\sigma}(\boldsymbol{x}, k)\hat{\Phi}(\boldsymbol{x}, k)e^{\mathbf{i}k\theta}, \tag{3.4}$$

where we take the following convention for the continuous Fourier transform

$$\hat{\phi}(\boldsymbol{x}, k) = (\mathcal{F}\phi)(\boldsymbol{x}, k) := \fint_0^{2\pi} \phi(\boldsymbol{x}, \theta)e^{-\mathbf{i}k\theta}\,\mathrm{d}\theta, \quad \phi = \Phi, \sigma. \tag{3.5}$$

Then the solution (3.2) can be reformulated as

$$\mathcal{F}\Phi = \mathcal{F}\mathcal{T}^{-1}\mu_s\mathcal{A}\Phi + \mathcal{F}\mathcal{T}^{-1}\mathcal{J}f. \tag{3.6}$$

When the scattering kernel σ is smooth (as we have assumed), a few Fourier modes of σ dominate, i.e.

$$\sigma(\boldsymbol{x}, \theta) \approx \sum_{k\in\mathbb{M}} \hat{\sigma}(\boldsymbol{x}, k)e^{\mathbf{i}k\theta}, \tag{3.7}$$

where $\mathbb{M} \subset \mathbb{Z}$ contains a small number of frequencies, typically centering at zero. Then the operator $\mathcal{A}$ can be approximated as

$$(\mathcal{A}\Phi)(\boldsymbol{x},\theta) \approx (\tilde{\mathcal{A}}\Phi)(\boldsymbol{x},\theta) := \sum_{k\in\mathbb{M}} e^{\mathbf{i}k\theta}\hat{\sigma}(\boldsymbol{x},k)\hat{\Phi}(\boldsymbol{x},k). \tag{3.8}$$

Noticing that integral of $\Phi(\boldsymbol{x},\theta)$ with respect to θ is the mean local density, which is usually important in application, we always assume $0 \in \mathbb{M}$. We introduce an operator as

$$(\mathcal{F}^\dagger\hat{\phi})(\boldsymbol{x},\theta) = \sum_{k\in\mathbb{M}} \hat{\phi}(\boldsymbol{x},k)e^{\mathbf{i}k\theta}, \tag{3.9}$$

which satisfies $\mathcal{F}\mathcal{F}^\dagger\hat{\phi} = \hat{\phi}$, similar as the pseudo-inverse in linear algebra. Therefore, we have $\tilde{\mathcal{A}}\Phi = \mathcal{F}^\dagger(\hat{\sigma}\hat{\Phi})$. Moreover, let $\hat{g}(\boldsymbol{x},k) = f(\boldsymbol{x})\delta_{k,0}$, then $\mathcal{J}f = \mathcal{F}^\dagger\hat{g}$.

Replacing $\mathcal{A}$ in (3.6) by $\tilde{\mathcal{A}}$ results in a Fredholm integral equation of the second kind with the following form

$$\hat{\Phi}(\boldsymbol{x},k) = \mathcal{K}\hat{\Phi}(\boldsymbol{x},k) + \tilde{\mathcal{K}}\hat{g}(\boldsymbol{x},k), \tag{3.10}$$

where the operators $\mathcal{K}$ and $\tilde{\mathcal{K}}$ are defined as

$$\mathcal{K} = \mathcal{F}\mathcal{T}^{-1}\mathcal{F}^\dagger\mu_s\hat{\sigma}, \quad \tilde{\mathcal{K}} = \mathcal{F}\mathcal{T}^{-1}\mathcal{F}^\dagger. \tag{3.11}$$

Noticing that

$$\begin{aligned}\tilde{\mathcal{K}}\hat{\phi}(\boldsymbol{x},k) &= \sum_{k'\in\mathbb{M}} \fint_0^{2\pi}\int_0^{\tau(\boldsymbol{x},\boldsymbol{v})} \exp\left(-\int_0^s \mu_t\left(\boldsymbol{x}-s'\boldsymbol{v}\right)ds'\right)\hat{\phi}(\boldsymbol{x}-s\boldsymbol{v},k)e^{\mathbf{i}(k'-k)\theta}\,\mathrm{d}s\,\mathrm{d}\theta \\ &= \sum_{k'\in\mathbb{M}}\int_\Omega \tilde{K}(\boldsymbol{x},\boldsymbol{y})e^{\mathbf{i}(k'-k)\theta}\hat{\phi}(\boldsymbol{y},k)\,\mathrm{d}\boldsymbol{y},\end{aligned} \tag{3.12}$$

where $\theta = \arccos\left(\frac{\boldsymbol{x}-\boldsymbol{y}}{|\boldsymbol{x}-\boldsymbol{y}|}\right)$, and $\tilde{K}(\boldsymbol{x},\boldsymbol{y})$ is the kernel for the isotropic case defined in (2.9), we have

$$\tilde{\mathcal{K}}\hat{\phi}(\boldsymbol{x},k) = \sum_{k'\in\mathbb{M}}\int_\Omega \tilde{K}(\boldsymbol{x},k,\boldsymbol{y},k')\hat{\phi}(\boldsymbol{y},k)\,\mathrm{d}\boldsymbol{y}, \quad \tilde{K}(\boldsymbol{x},k,\boldsymbol{y},k') = \tilde{K}(\boldsymbol{x},\boldsymbol{y})e^{\mathbf{i}(k'-k)\theta}, \tag{3.13}$$

and

$$\mathcal{K}\hat{\phi}(\boldsymbol{x},k) = \sum_{k'\in\mathbb{M}}\int_\Omega K(\boldsymbol{x},k,\boldsymbol{y},k')\hat{\phi}(\boldsymbol{y},k)\,\mathrm{d}\boldsymbol{y}, \quad K(\boldsymbol{x},k,\boldsymbol{y},k') = K(\boldsymbol{x},\boldsymbol{y})\hat{\sigma}(\boldsymbol{y},k')e^{\mathbf{i}(k-k')\theta}, \tag{3.14}$$

where $K(\boldsymbol{x},\boldsymbol{y})$ is the kernel defined in (2.10). The kernel $\tilde{K}$ is Hermitian while K is not due to the existence of $\mu_s(\boldsymbol{y})\hat{\sigma}(\boldsymbol{y},k')$. If $|\hat{\sigma}(\boldsymbol{y},k')|$ is uniformly positive for any $k' \in \mathbb{M}$, i.e. there exists a $c_0 > 0$ such that $|\hat{\sigma}(\boldsymbol{y},k')| \geq c_0$ for any $k' \in \mathbb{M}$, one can use the same technique as in (2.11) to obtain a Hermitian operator. However, the condition $\hat{\sigma}(\boldsymbol{y},k') > 0$ for any $k' \in \mathbb{M}$, $\boldsymbol{y} \in \Omega$ is usually too strong to hold in general.

3.1.2. 3D case

For the case $d = 3$, $\boldsymbol{v} = (\sin(\theta)\cos(\psi), \sin(\theta)\sin(\psi), \cos(\theta))$. Expressing the spherical function $\Phi(\boldsymbol{x},\boldsymbol{v})$ and $\sigma(\boldsymbol{x},\theta)$ in terms of the spherical harmonic basis, we obtain

$$\begin{aligned}\Phi(\boldsymbol{x},\boldsymbol{v}) &= \sum_{l=0}^{\infty}\sum_{m=-l}^{l}\hat{\Phi}(\boldsymbol{x},l,m)Y_l^m(\theta,\psi), \\ \sigma(\boldsymbol{x},\theta) &= \sum_{l=0}^{\infty}\hat{\sigma}(\boldsymbol{x},l)Y_l^0(\theta),\end{aligned} \tag{3.15}$$

where $Y_l^m(\theta,\psi)$ is the spherical harmonic basis, and

$$\hat{\phi}(\boldsymbol{x},l,m) = \mathcal{F}\phi(\boldsymbol{x},l,m) := \frac{1}{4\pi}\int_0^{2\pi}\int_0^{\pi}\phi(\boldsymbol{x},\theta,\psi)Y_l^m(\theta,\psi)\,\mathrm{d}\theta\,\mathrm{d}\psi, \quad \phi = \Phi,\sigma. \tag{3.16}$$

Then the operator $\mathcal{A}$ can be expressed as

$$(\mathcal{A}\Phi)(\boldsymbol{x},\boldsymbol{v})=\sum_{l=0}^{\infty}\sum_{m=-l}^{l}\hat{\Phi}(\boldsymbol{x},l,m)\hat{\sigma}(\boldsymbol{x},l)\sqrt{\frac{4\pi}{2l+1}}Y_l^m(\theta,\psi). \tag{3.17}$$

Similar to the $d=2$ case, if a few modes of σ dominate, i.e.

$$\sigma(\boldsymbol{x},\theta)\approx\sum_{l\in\mathbb{M}}\hat{\sigma}(\boldsymbol{x},l)Y_l^m(\theta,\psi), \tag{3.18}$$

the operator $\mathcal{A}$ can be approximated by

$$(\mathcal{A}\Phi)(\boldsymbol{x},\boldsymbol{v})\approx\tilde{\mathcal{A}}\Phi(\boldsymbol{x},\boldsymbol{v}):=\sum_{l\in\mathbb{M}}\sum_{m=-l}^{l}\hat{\Phi}(\boldsymbol{x},l,m)\hat{\sigma}(\boldsymbol{x},l)\sqrt{\frac{4\pi}{2l+1}}Y_l^m(\theta,\psi). \tag{3.19}$$

Similar to the derivation of the $d=2$ case, by replacing $\mathcal{A}$ by $\tilde{\mathcal{A}}$, one obtains a Fredholm integral equation of the second kind with the form

$$\hat{\Phi}(\boldsymbol{x},l,m)=\mathcal{K}_A\hat{\Phi}(\boldsymbol{x},l,m)+\tilde{\mathcal{K}}\hat{g}(\boldsymbol{x},l,m), \tag{3.20}$$

where $\hat{g}(\boldsymbol{x},l,m)=f(\boldsymbol{x})\delta_{l,0}\delta_{m,0}$, and the operators $\mathcal{K}$ and $\tilde{\mathcal{K}}$ are defined as

$$\begin{aligned}\mathcal{K}\hat{\phi}(\boldsymbol{x},l,m)&=\sum_{l'\in\mathbb{M}}\sum_{m'=-l'}^{l'}\int_{\Omega}K(\boldsymbol{x},l,m,\boldsymbol{y},l',m')\hat{\phi}(\boldsymbol{y},l',m')\,\mathrm{d}\boldsymbol{x},\\ K(\boldsymbol{x},l,m,\boldsymbol{y},l',m')&=K(\boldsymbol{x},\boldsymbol{y})\hat{\sigma}(\boldsymbol{y},l')\sqrt{\frac{4\pi}{2l+1}}Y_l^m(\theta,\psi)Y_{l'}^{m'}(\theta,\psi),\end{aligned} \tag{3.21}$$

and

$$\begin{aligned}\tilde{\mathcal{K}}\hat{\phi}(\boldsymbol{x},l,m)&=\sum_{l'\in\mathbb{M}}\sum_{m'=-l'}^{l'}\int_{\Omega}\tilde{K}(\boldsymbol{x},l,m,\boldsymbol{y},l',m')\hat{\phi}(\boldsymbol{y},l,m)\,\mathrm{d}\boldsymbol{x},\\ \tilde{K}(\boldsymbol{x},l,m,\boldsymbol{y},l',m')&=\tilde{K}(\boldsymbol{x},\boldsymbol{y})Y_l^m(\theta,\psi)Y_{l'}^{m'}(\theta,\psi).\end{aligned} \tag{3.22}$$

We remark that if $\mathbb{M}=\{0\}$, then the Fredholm equations (3.10) and (3.20) simplify to the ones in the isotropic scattering case.

Here we point out that in the plane-parallel geometry, i.e., homogeneous in y and z directions, the integral equation (3.20) degenerates into the case in [14], where the scattering term is expanded into Legendre polynomials.

3.2. Existence theory

In this subsection, we extend the existence theory for the isotropic case to the anisotropic one. For simplicity, here we only study the case $d=2$, and all the conclusions in this subsection hold for the $d=3$ case.

Define the vector function space $L^p(\Omega,\mathbb{M})$ with $1\le p\le\infty$ as

$$L^p(\Omega,\mathbb{M}):=\left\{\boldsymbol{v}:\Omega\to\mathbb{C}^{|\mathbb{M}|}\text{ such that }\boldsymbol{v}(x)=(v_m(x))_{m\in\mathbb{M}}:v_m\in L^p(\Omega)\right\}, \tag{3.23}$$

where $|\mathbb{M}|$ denotes the number of modes in set $\mathbb{M}$, and the norm is given by

$$\|\boldsymbol{v}\|_{L^p(\Omega,\mathbb{M})}=\left(\int_{\Omega}\|\boldsymbol{v}(x)\|_{l^2}^p\,dx\right)^{1/p}=\left(\int_{\Omega}\left(\sum_{i=1}^{|\mathbb{M}|}|v_i(x)|^2\right)^{p/2}dx\right)^{1/p}. \tag{3.24}$$

We also introduce the assumption:

(C3) $\sigma(\boldsymbol{x},\boldsymbol{v}\cdot\boldsymbol{v}')$ is non-negative and measurable and

$$⨍_{\mathbb{S}^{d-1}}\sigma(\boldsymbol{x},\boldsymbol{v}\cdot\boldsymbol{v}')\,\mathrm{d}\boldsymbol{v}'=1,\quad\text{for any }(\boldsymbol{x},\boldsymbol{v})\in\Omega\times\mathbb{S}^{d-1}. \tag{3.25}$$

The main analytic result in the anisotropic case is the following theorem.

Theorem 2. *Under assumptions (C1), (C2) and (C3), for any $1 \le p \le \infty$ and $f \in L^p(\Omega)$, the Fredholm equation (3.10) admits a unique solution $\hat{\Phi} \in L^p(\Omega, \mathbb{M})$ which satisfies*

$$\left\| \hat{\Phi} \right\|_{L^p(\Omega,\mathbb{M})} \le \tau \exp\left(\tau \, \|\mu_s\|_{L^\infty(\Omega)}\right) \|f\|_{L^p(\Omega)}. \tag{3.26}$$

The proof is similar to that of Theorem 1. Before the proof, we first define

$$G(k,k';\boldsymbol{x}) = \fint_0^{2\pi} \int_0^{\tau(\boldsymbol{x},\boldsymbol{v})} E^{[\mu_t]}(\boldsymbol{x},\boldsymbol{v},s)\mu_s(\boldsymbol{x}) e^{\mathbf{i}(k'-k)\theta} \, \mathrm{d}s \, \mathrm{d}\theta,$$

and the matrix function $\mathbf{G}(\boldsymbol{x}) = (G(k,k';\boldsymbol{x}))$. For any given $\boldsymbol{w} \in \mathbb{C}^{|\mathbb{M}|}$, a direct calculation yields

$$\boldsymbol{w}^H \mathbf{G} \boldsymbol{w} = \fint_0^{2\pi} \int_0^{\tau(\boldsymbol{x},\boldsymbol{v})} E^{[\mu_t]}(\boldsymbol{x},\boldsymbol{v},s)\mu_s(\boldsymbol{x}) \sum_{k\in\mathbb{M}} w_k^* e^{-\mathbf{i}k\theta} \sum_{k'\in\mathbb{M}} w_{k'} e^{\mathbf{i}k'\theta} \, \mathrm{d}s \, \mathrm{d}\theta \le C \fint_0^{2\pi} \left| \sum_{k\in\mathbb{M}} w_k e^{\mathbf{i}k\theta} \right|^2 \mathrm{d}\theta = C|\boldsymbol{w}|^2,$$

where the relation (2.16), is used in the inequality. Therefore, we obtain

$$\|\mathbf{G}\|_2 \le C < 1, \tag{3.27}$$

where $\|\cdot\|_2$ is the 2-norm of a matrix.

Similar to the isotropic case, we first study the case $p = \infty$ and obtain the following result.

Lemma 3. *Under assumptions (C1), (C2) and (C3), the linear operator $\mathcal{K} : L^\infty(\Omega,\mathbb{M}) \to L^\infty(\Omega,\mathbb{M})$ is a contraction map with*

$$\|\mathcal{K}\|_{L^\infty(\Omega,\mathbb{M})\to L^\infty(\Omega,\mathbb{M})} \le C < 1. \tag{3.28}$$

Assume $f \in L^\infty(\Omega)$ and let $\hat{g}(\boldsymbol{x},k) = f(\boldsymbol{x})\delta_{k,0}$, then

$$\left\| \tilde{\mathcal{K}}\hat{g} \right\|_{L^\infty(\Omega,\mathbb{M})} \le \tau \, \|f\|_{L^\infty(\Omega)}. \tag{3.29}$$

Proof. The condition (C3) indicates $|\hat{\sigma}(\boldsymbol{x},k)| \le 1$, $k \in \mathbb{M}$. For any $\hat{\boldsymbol{\phi}} \in L^\infty(\Omega,\mathbb{M})$, recalling (3.12) and $|\hat{\sigma}(\boldsymbol{x},k)| \le 1$, we have

$$\begin{aligned}
|(\mathcal{K}\hat{\phi})(\boldsymbol{x},k)| &= \left| \fint_0^{2\pi} \int_0^{\tau(\boldsymbol{x},\boldsymbol{v})} E^{[\mu_t]}(\boldsymbol{x},\boldsymbol{v},s)\mu_s(\boldsymbol{x}-s\boldsymbol{v}) \sum_{k'\in\mathbb{M}} \hat{\phi}(\boldsymbol{x}-s\boldsymbol{v},k')\hat{\sigma}(\boldsymbol{x}-s\boldsymbol{v},k') e^{\mathbf{i}(k'-k)\theta} \, \mathrm{d}s \, \mathrm{d}\theta \right| \\
&\le \sum_{k'\in\mathbb{M}} G(k,k';\boldsymbol{x}) \left\| \hat{\sigma}(\boldsymbol{x},k')\hat{\phi}(\boldsymbol{x},k') \right\|_{L^\infty(\Omega)} \le \sum_{k'\in\mathbb{M}} G(k,k';\boldsymbol{x}) \left\| \hat{\phi}(\boldsymbol{x},k') \right\|_{L^\infty(\Omega)} \\
&\le C \left\| \hat{\boldsymbol{\phi}} \right\|_{L^\infty(\Omega,\mathbb{M})}.
\end{aligned}$$

Therefore, the operator $\mathcal{K}$ is a contraction map in $L^\infty(\Omega,\mathbb{M})$ with $\|\mathcal{K}\|_{L^p(\Omega,\mathbb{M})\to L^p(\Omega,\mathbb{M})} \le C$.

The definition of $\tilde{\mathcal{K}}$ indicates

$$|(\tilde{\mathcal{K}}\hat{g})(\boldsymbol{x},k)| = \left| \int_\Omega \tilde{K}(\boldsymbol{x},\boldsymbol{y}) e^{-\mathbf{i}k\theta} f(\boldsymbol{y}) \, \mathrm{d}\boldsymbol{y} \right| \le \int_\Omega \tilde{K}(\boldsymbol{x},\boldsymbol{y}) |f(\boldsymbol{y})| \, \mathrm{d}\boldsymbol{y} = \tilde{\mathcal{K}}|f| \le \tau \, \|f\|_{L^\infty(\Omega)},$$

where (2.14) is used in the last inequality. □

For the case $1 \le p < \infty$, notice that (3.10) can be rewritten as $\hat{\Phi} = \tilde{\mathcal{K}}\left(\mu_s\hat{\sigma}\hat{\Phi} + \hat{g}\right)$ with $\hat{g}(\boldsymbol{x},k) = f(\boldsymbol{x})\delta_{k,0}$. By letting $\hat{\Psi} = \mu_s\hat{\sigma}\hat{\Phi} + \hat{g}$, the Fredholm equation (3.10) can be stated equivalently as

$$\hat{\Psi}(\boldsymbol{x},k) = \mu_s\hat{\sigma}\tilde{\mathcal{K}}\hat{\Psi}(\boldsymbol{x},k) + \hat{g}, \quad \hat{\Phi} = \tilde{\mathcal{K}}\hat{\Psi}. \tag{3.30}$$

Lemma 4. *Under assumptions (C1), (C2) and (C3), the linear operator $\mu_s\hat{\sigma}\tilde{\mathcal{K}} : L^p(\Omega,\mathbb{M}) \to L^p(\Omega,\mathbb{M})$, $1 \le p < \infty$ is a contraction map with*

$$\left\| \mu_s\hat{\sigma}\tilde{\mathcal{K}} \right\|_{L^p(\Omega,\mathbb{M})\to L^p(\Omega,\mathbb{M})} \le C, \tag{3.31}$$

and

$$\left\|\hat{\Phi}\right\|_{L^p(\Omega,\mathbb{M})} \le \tau \left\|\hat{\Psi}\right\|_{L^p(\Omega,\mathbb{M})}. \tag{3.32}$$

Proof. For any $\hat{\phi} \in L^p(\Omega,\mathbb{M})$, since $|\hat{\sigma}(\boldsymbol{x},k)| \le 1$, we have $\left\|\mu_s\hat{\sigma}\tilde{\mathcal{K}}\hat{\phi}\right\|_{L^p(\Omega,\mathbb{M})} \le \left\|\mu_s\tilde{\mathcal{K}}\hat{\phi}\right\|_{L^p(\Omega,\mathbb{M})}$, and

$$\begin{aligned}\left\|\mu_s\tilde{\mathcal{K}}\hat{\phi}\right\|_{L^p(\Omega,\mathbb{M})} &= \left\|\sum_{k'\in\mathbb{M}} \fint_0^{2\pi}\int_0^{\tau(\boldsymbol{x},\boldsymbol{v})} E^{[\mu_t]}(\boldsymbol{x},\boldsymbol{v},s)\mu_s(\boldsymbol{x})e^{\mathbf{i}(k'-k)\theta}\hat{\phi}(\boldsymbol{x}-s\boldsymbol{v},k')\,\mathrm{d}s\,\mathrm{d}\theta\right\|_{L^p(\Omega,\mathbb{M})}\\ &= \left\|\sum_{k'\in\mathbb{M}} G(k,k';\boldsymbol{x})\hat{\phi}(\boldsymbol{x},k')\right\|_{L^p(\Omega,\mathbb{M})} \le C\left\|\hat{\phi}\right\|_{L^p(\Omega,\mathbb{M})},\end{aligned}$$

where the relation (3.27) is used in the last inequality. Therefore, $\mu_s\hat{\sigma}\tilde{\mathcal{K}}$ is a contraction map in $L^p(\Omega,\mathbb{M})$ and $\left\|\mu_s\hat{\sigma}\tilde{\mathcal{K}}\right\|_{L^p(\Omega,\mathbb{M})\to L^p(\Omega,\mathbb{M})} \le C$.

The non-negativeness of μ_t indicates $0 \le E^{[\mu_t]}(\boldsymbol{x},\boldsymbol{v},s) \le 1$. Let

$$G_2(k,k';\boldsymbol{x}) = \fint_0^{2\pi}\int_0^{\tau(\boldsymbol{x},\boldsymbol{v})} E^{[\mu_t]}(\boldsymbol{x},\boldsymbol{v},s)e^{\mathbf{i}(k'-k)\theta}\,\mathrm{d}s\,\mathrm{d}\theta$$

and the matrix function $\mathbf{G}_2 = (G_2(k,k';\boldsymbol{x}))$, then using the same method in studying the matrix $\mathbf{G}$, we can obtain that $\|\mathbf{G}_2\|_2 \le \tau$. A direct calculation yields

$$\begin{aligned}\left\|\hat{\Phi}\right\|_{L^p(\Omega,\mathbb{M})} &= \left\|\sum_{k'\in\mathbb{M}} \fint_0^{2\pi}\int_0^{\tau(\boldsymbol{x},\boldsymbol{v})} E^{[\mu_t]}(\boldsymbol{x},\boldsymbol{v},s)e^{\mathbf{i}(k'-k)\theta}\,\mathrm{d}s\,\mathrm{d}\boldsymbol{v}\hat{\Psi}(\boldsymbol{x},k')\right\|_{L^p(\Omega,\mathbb{M})}\\ &= \left\|\mathbf{G}_2\hat{\Psi}\right\|_{L^p(\Omega,\mathbb{M})} \le \tau\left\|\hat{\Psi}\right\|_{L^p(\Omega,\mathbb{M})}. \quad \square\end{aligned} \tag{3.33}$$

With these two lemmas, the Theorem 2 goes as follows.

Proof of Theorem 2. This proof is similar to the proof of Theorem 1. For the case $p=\infty$, noticing Lemma 3, and applying Banach's fixed point theorem [23, Chapter 3, Theorem 3.2], we obtain that (3.10) has a unique solution $\hat{\Phi} \in L^\infty(\Omega,\mathbb{M})$ if $\mathcal{K}\hat{g} \in L^\infty(\Omega,\mathbb{M})$, which is guaranteed by (3.29).

For the case $1 \le p < \infty$, noticing Lemma 4 and applying Banach's fixed point theorem, we obtain that (3.30) has a unique solution $\hat{\Psi} \in L^p(\Omega,\mathbb{M})$, which indicates (3.10) has a unique solution $\hat{\Phi} \in L^p(\Omega,\mathbb{M})$. The conclusion (3.26) is a directly deduction of Lemma 4. This completes the proof. $\square$

By setting $p=2$ in Lemma 4, we can directly deduce the result.

Corollary 2. *Under assumptions (C1), (C2) and (C3), the linear operator $\mathcal{I}-\mathcal{K}$: $L^2(\Omega,\mathbb{M}) \to L^2(\Omega,\mathbb{M})$ is positive definite.*

Proof. Since σ is a real function, the operator $\mu_s\hat{\sigma}$ is a Hermitian operator. Noticing $\mathcal{K} = \tilde{\mathcal{K}}\mu_s\hat{\sigma}$, and $\tilde{\mathcal{K}}$ is a Hermitian operator, for any $\phi \in L^2(\Omega,\mathbb{M})$, we have

$$\langle\phi,\mathcal{K}\phi\rangle = \left\langle\tilde{\mathcal{K}}\phi,\mu_s\hat{\sigma}\phi\right\rangle = \left\langle\mu_s\hat{\sigma}\tilde{\mathcal{K}}\phi,\phi\right\rangle.$$

Using (3.31) with $p=2$ and Hölder inequality, we can obtain

$$\left\langle\phi,\mu_s\tilde{\sigma}\tilde{\mathcal{K}}\phi\right\rangle \le C\|\phi\|^2_{L^2(\Omega,\mathbb{M})},$$

so

$$\langle\phi,(\mathcal{I}-\mathcal{K})\phi\rangle \le (1-C)\|\phi\|^2_{L^2(\Omega,\mathbb{M})},$$

i.e. the operator $\mathcal{I}-\mathcal{K}$ is positive definite. $\square$

3.3. Fast algorithms

In this subsection, we study the fast algorithms for the Fredholm equations (3.10) and (3.20) and take the $2D$ case (3.10) as the example. The framework of the algorithm can be split into 2 steps:

T.1 Evaluate $(\tilde{\mathcal{K}} f)(\boldsymbol{x}, k)$;
T.2 Given $\hat{r}(\boldsymbol{x}, k)$, solve $(\mathcal{I} - \mathcal{K})\,\hat{\Phi}(\boldsymbol{x}, k) = \hat{r}(\boldsymbol{x}, k)$, or equivalently $\hat{\Phi}(\boldsymbol{x}, k) = (\mathcal{I} - \mathcal{K})^{-1}\,\hat{r}(\boldsymbol{x}, k)$.

Following the discretization scheme used in the isotropic case, we introduce $u_{i,k}$ as an approximation of $\hat{\Phi}(\boldsymbol{x}_i, k)$, $\mu_{s,i} = \mu_s(\boldsymbol{x}_i)$, and $f_i = f(\boldsymbol{x}_i)$. The discretization of anisotropic integral equations takes the form

$$u_{i,k} = \sum_{k' \in \mathbb{M}} \sum_{j=1}^{N} K_{i,k,j,k'} u_{j,k'} + \sum_{j=1}^{N} K_{i,k,j,0} \frac{f_j}{\mu_{s,j}}. \tag{3.34}$$

For $K_{i,k,j,k'}$, where $i \neq j$, $K_{i,k,j,k'}$ is equal to the product of $K(\boldsymbol{x}_i, k, \boldsymbol{x}_j, k')$ and the cell volume. When $i = j$, since $K(\boldsymbol{x}, k, \boldsymbol{y}, k')$ is singular at $\boldsymbol{x} = \boldsymbol{y}$ the value $K_{i,k,i,k'}$ is set to be integral of K at the i-th cell. The treatments of the line integral in $E(\boldsymbol{x}, \boldsymbol{y})$ and the integral of $K(\boldsymbol{x}, \boldsymbol{y})$ in a cell are the same as those of the isotropic case.

If one writes $u_{i,k}$ as a vector $\boldsymbol{u} \in \mathbb{C}^{NM}$ and $K_{i,k,j,k'}$ into a matrix form $\mathbf{K} \in \mathbb{C}^{NM \times NM}$, then (3.34) can be written as

$$\mathbf{A}\boldsymbol{u} = \mathbf{K}\boldsymbol{f}, \tag{3.35}$$

where $\mathbf{A} = \mathbf{I} - \mathbf{K}$ and $\boldsymbol{f}$ is the vector form of $f_i \delta_{k,0}/\mu_{s,i}$. Corollary 2 guarantees the matrix $\mathbf{A}$ is positive definite.

Similar to the isotropic case, in order to solve (3.35), a direct method that factorizes $\mathbf{A}$ by LU or Cholesky decomposition takes $O((NM)^3)$ steps and in what follows we discuss two fast algorithms for both homogeneous and inhomogeneous media.

3.3.1. Homogeneous media and FFT-based algorithm

For a homogeneous medium, the total transport coefficient μ_t and the scattering coefficient μ_s are independent on $\boldsymbol{x}$. As a result, the kernel

$$K(\boldsymbol{x}, k, \boldsymbol{y}, k') = \frac{\mu_s \hat{\sigma}(k')}{|\mathbb{S}^{d-1}|} \frac{\exp(-\mu_t |\boldsymbol{x} - \boldsymbol{y}|)}{|\boldsymbol{x} - \boldsymbol{y}|} e^{\mathbf{i}(k'-k)\theta} := \kappa(\boldsymbol{x} - \boldsymbol{y}, k, k') \tag{3.36}$$

with $\theta = \arccos\left(\frac{\boldsymbol{x}-\boldsymbol{y}}{|\boldsymbol{x}-\boldsymbol{y}|}\right)$ depends only on $\boldsymbol{x} - \boldsymbol{y}$, k and k'. Hence the integral part

$$C(\boldsymbol{x}, k, k') := \int_{\Omega} \kappa(\boldsymbol{x} - \boldsymbol{y}, k, k') \hat{g}(\boldsymbol{y}, k')\, \mathrm{d}\boldsymbol{y} \tag{3.37}$$

of $(\mathcal{K}\hat{g})(\boldsymbol{x}, k)$ is a convolution. Similar to the isotropic case, if the domain Ω is rectangular, the FFT-based algorithm in Section 2.3.1 can be applied to the evaluation of $C(\boldsymbol{x}, k, k')$ for each $k, k' \in \mathbb{M}$. Thus, in order to evaluate $(\mathcal{K}\hat{g})(\boldsymbol{x}, k)$, one just needs to use the FFT-based algorithm in Section 2.3.1 to calculate $C(\boldsymbol{x}, k, k')$ for each $k, k' \in \mathbb{M}$ and then $(\mathcal{K}\hat{g})(\boldsymbol{x}, k) = \sum_{k' \in \mathbb{M}} G(\boldsymbol{x}, k, k')$. Once one has the algorithm of applying $(\mathcal{K}\hat{g})(\boldsymbol{x}, k)$, Step T.2 can be solved by iterative methods, for example GMRES [33].

If one discretizes the domain uniformly by n points in each direction, the computation cost to evaluate $(\mathcal{K}\hat{g})(\boldsymbol{x}, k)$ is reduced to $O(M^2 N \log(N))$ with $N = n^d$ and $M = |\mathbb{M}|$. Hence, the computation costs of Steps T.1 and T.2 are $O(M^2 N \log(N))$ and $(n_{iter} M^2 N \log(N))$, respectively, where n_{iter} is the number of iteration steps in the iterative method. So the total computation cost is $O(n_{iter} M^2 N \log(N))$. Before the evaluation of $(\mathcal{K}\hat{g})(\boldsymbol{x}, k)$, one needs to calculate the Fourier modes of $\kappa(\boldsymbol{x}, k, k')$ for each $k, k' \in \mathbb{M}$, so the computation cost and storage memory of the precomputation are $O(M^2 N \log(N))$ and $O(M^2 N)$, respectively.

We remark that the algorithm presented above can be directly applied on (3.20). The only difference is M, which equals to $M = \sum_{l \in \mathbb{M}} (2l + 1)$ for $3D$ case.

Another issue worth to remark is that the summation with respect to k' in the evaluation of $\mathcal{K}\hat{g}$ can be also accelerated by FFT if M is not small. The primary idea is that one can first calculate $\hat{\sigma}\,\hat{g}$ and then the residue of the kernel $K(\boldsymbol{x}, k, \boldsymbol{y}, k')$ only depends on $\boldsymbol{x} - \boldsymbol{y}$ and $k - k'$.

3.3.2. Inhomogeneous media and RSF-based algorithm

As is discussed in Section 2.3.2, the FFT-based algorithm requires the total transport coefficient μ_t be constant and the iterative method is used to solve Step T.2. For a inhomogeneous medium, the RSF-based algorithm in Section 2.3.2 does not suffer from these limitations. Here we apply RSF on the system (3.35).

One important issue is how to apply the RSF to the matrix $\mathbf{A}$. RSF needs to select the skeletonization to approximate the factorization. A nature choice is for different Fourier modes at the same position $\boldsymbol{x}$ to use the same skeletonization.

Table 7
Anisotropic scattering case: computational cost of the three methods for different n and ϵ with constant scattering coefficient $\mu_s = 1$ and transport coefficient $\mu_t = 1.2$.

n	ϵ	$T_{\text{pre}}^{\text{DIR}}$ (sec)	$T_{\text{pre}}^{\text{FFT}}$ (sec)	$T_{\text{pre}}^{\text{RSF}}$ (sec)	$T_{\text{sol}}^{\text{DIR}}$ (sec)	$T_{\text{sol}}^{\text{FFT}}$ (sec)	$T_{\text{sol}}^{\text{RSF}}$ (sec)
32	$1E{-}4$	$2.42E{+}0$	$1.33E{-}3$	$1.84E{+}0$	$4.16E{-}2$	$2.05E{-}2$	$3.32E{-}2$
64	$1E{-}4$	$6.15E{+}1$	$1.23E{-}2$	$1.69E{+}1$	$6.28E{-}1$	$6.54E{-}2$	$6.87E{-}2$
128	$1E{-}4$	–	$7.84E{-}2$	$1.21E{+}2$	–	$1.31E{-}1$	$3.17E{-}1$
256	$1E{-}4$	–	$3.35E{-}1$	$8.24E{+}2$	–	$6.87E{-}1$	$1.53E{+}0$
32	$1E{-}6$	$2.42E{+}0$	$1.33E{-}3$	$3.57E{+}0$	$4.16E{-}2$	$2.46E{-}2$	$1.98E{-}2$
64	$1E{-}6$	$6.15E{+}1$	$1.23E{-}2$	$3.48E{+}1$	$6.28E{-}1$	$6.99E{-}2$	$1.11E{-}1$
128	$1E{-}6$	–	$7.84E{-}2$	$3.08E{+}2$	–	$1.47E{-}1$	$5.77E{-}1$
256	$1E{-}6$	–	$3.35E{-}1$	$2.71E{+}3$	–	$1.20E{+}0$	$3.29E{+}0$
32	$1E{-}8$	$2.42E{+}0$	$1.33E{-}3$	$3.83E{+}0$	$4.16E{-}2$	$2.67E{-}2$	$2.60E{-}2$
64	$1E{-}8$	$6.15E{+}1$	$1.23E{-}2$	$5.93E{+}1$	$6.28E{-}1$	$8.45E{-}2$	$1.59E{-}1$
128	$1E{-}8$	–	$7.84E{-}2$	$5.80E{+}2$	–	$1.69E{-}1$	$8.62E{-}1$
256	$1E{-}8$	–	$3.35E{-}1$	$4.88E{+}3$	–	$1.67E{+}0$	$6.02E{+}0$

Table 8
Anisotropic scattering case: relative error of the FFT-based method and RSF-based method for three source term in (2.26) with constant scattering coefficient $\mu_s = 1$ and transport coefficient $\mu_t = 1.2$. $\mathcal{E}_k$ is the relative error for the source term f_k, $k = 1, 2, 3$.

n	ϵ	$\mathcal{E}_1^{\text{FFT}}$	$\mathcal{E}_1^{\text{RSF}}$	$\mathcal{E}_2^{\text{FFT}}$	$\mathcal{E}_2^{\text{RSF}}$	$\mathcal{E}_3^{\text{FFT}}$	$\mathcal{E}_3^{\text{RSF}}$
32	$1E{-}4$	$8.15E{-}6$	$2.49E{-}5$	$2.18E{-}5$	$2.55E{-}5$	$3.11E{-}5$	$2.19E{-}5$
64	$1E{-}4$	$8.30E{-}6$	$8.28E{-}5$	$2.26E{-}5$	$8.34E{-}5$	$3.18E{-}5$	$7.67E{-}5$
128	$1E{-}4$	$2.94E{-}4$	$3.36E{-}4$	$2.28E{-}5$	$3.34E{-}4$	$3.20E{-}5$	$2.65E{-}4$
256	$1E{-}4$	$2.95E{-}4$	$1.34E{-}3$	$5.92E{-}4$	$1.23E{-}3$	$3.22E{-}5$	$9.64E{-}4$
32	$1E{-}6$	$3.75E{-}7$	$3.20E{-}7$	$7.57E{-}7$	$3.11E{-}7$	$6.11E{-}8$	$2.89E{-}7$
64	$1E{-}6$	$3.89E{-}7$	$1.06E{-}6$	$7.77E{-}7$	$1.13E{-}6$	$9.44E{-}7$	$9.54E{-}7$
128	$1E{-}6$	$3.93E{-}7$	$3.58E{-}6$	$7.78E{-}7$	$3.72E{-}6$	$9.51E{-}7$	$3.15E{-}6$
256	$1E{-}6$	$3.94E{-}7$	$1.20E{-}5$	$7.78E{-}7$	$1.16E{-}5$	$9.52E{-}7$	$9.07E{-}6$
32	$1E{-}8$	$3.20E{-}10$	$4.36E{-}9$	$1.28E{-}9$	$4.52E{-}9$	$1.88E{-}9$	$4.00E{-}9$
64	$1E{-}8$	$8.36E{-}9$	$2.18E{-}8$	$1.42E{-}9$	$2.29E{-}8$	$1.99E{-}9$	$1.99E{-}8$
128	$1E{-}8$	$8.41E{-}9$	$5.44E{-}8$	$1.45E{-}9$	$5.69E{-}8$	$2.01E{-}9$	$4.69E{-}8$
256	$1E{-}8$	$8.41e-9$	$1.52E{-}7$	$5.19E{-}8$	$1.53E{-}7$	$6.07E{-}8$	$1.32E{-}7$

However, the different Fourier modes of σ may differ from others significantly. In this case, using the same skeletonization at each position is not always the optimal choice. Here we regard *the pair of a position and a Fourier mode* as a *generalized point*, and select the skeletonization over such generalized points. As a result, the Fourier modes selected at different points can vary.

As the size of the matrix is now NM, the precomputation (factorization) cost of RSF is t_f in (2.24), with N replaced with NM. The computation cost of Steps T.1 and T.2 are both $t_{a/s}$ in (2.24) also with N replaced with NM.

Finally, we remark that the RSF-based algorithm can be also directly applied on (3.20) without any difficulty.

3.4. Numerical results

This subsection performs numerical simulations for the anisotropic scattering case and reports the results for different n, different tolerance ϵ, and also different choices of the coefficients μ_s and μ_t.

3.4.1. Homogeneous media

Here the scattering kernel σ is chosen to be

$$\sigma(\theta) = 1 + \frac{1}{5}e^{\mathbf{i}\theta} + \frac{1}{5}e^{-\mathbf{i}\theta}, \tag{3.38}$$

and accordingly $\mathbb{M} = \{-1, 0, 1\}$. The absorption coefficient $\mu_a = \mu_t - \mu_s$ is always set as $\mu_a = 0.2$.

Computational cost Similar to the isotropic case, we perform simulations for different mesh sizes $n = 32$, 64, 128 and 256 and different tolerance ϵ as $1E{-}4$, $1E{-}6$ and $1E{-}8$, for the constant scattering coefficients $\mu_s = 1$ and $\mu_t = 1.2$. The results are presented in Table 7 with the source term set to (2.26a). All the conclusions for the isotropic case hold for this case.

Relative error Table 8 presents the relative error of the FFT-based method and the RSF-based method for three source terms (2.26) with $\mu_s = 1$ and $\mu_t = 1.2$. The reference solution is obtained with the direct method if $n = 32$ and 64 and with the

Table 9
Anisotropic scattering case: computational cost and relative error for different scattering coefficient μ_s and ϵ with $n = 128$ and $\mu_t = \mu_s + 0.2$.

μ_s	ϵ	$T_{\text{pre}}^{\text{FFT}}$	$T_{\text{pre}}^{\text{RSF}}$	$T_{\text{sol}}^{\text{FFT}}$	$T_{\text{sol}}^{\text{RSF}}$	$\mathcal{E}^{\text{FFT}}$	$\mathcal{E}^{\text{RSF}}$
1	$1E{-}4$	$1.40E{-}2$	$1.78E{+}1$	$5.65E{-}2$	$7.97E{-}2$	$8.30E{-}6$	$9.70E{-}5$
10	$1E{-}4$	$1.55E{-}2$	$1.67E{+}1$	$9.29E{-}2$	$7.09E{-}2$	$4.93E{-}5$	$8.18E{-}4$
100	$1E{-}4$	$1.33E{-}2$	$1.17E{+}1$	$1.04E{-}1$	$5.74E{-}2$	$1.10E{-}4$	$5.40E{-}5$
1	$1E{-}6$	$1.34E{-}2$	$3.65E{+}1$	$5.92E{-}2$	$1.11E{-}1$	$3.89E{-}7$	$1.07E{-}6$
10	$1E{-}6$	$1.38E{-}2$	$3.75E{+}1$	$1.55E{-}1$	$1.18E{-}1$	$1.31E{-}7$	$4.73E{-}6$
100	$1E{-}6$	$1.34E{-}2$	$2.12E{+}1$	$1.63E{-}1$	$6.33E{-}2$	$8.40E{-}7$	$7.11E{-}7$
1	$1E{-}8$	$1.31E{-}2$	$6.26E{+}1$	$8.51E{-}2$	$1.64E{-}1$	$8.36E{-}9$	$1.81E{-}8$
10	$1E{-}8$	$1.51E{-}2$	$6.13E{+}1$	$1.81E{-}1$	$1.67E{-}1$	$2.64E{-}9$	$5.02E{-}8$
100	$1E{-}8$	$1.41E{-}2$	$4.02E{+}1$	$2.23E{-}1$	$1.20E{-}1$	$1.17E{-}8$	$8.48E{-}9$

Table 10
Anisotropic scattering case: computational cost of the direct method and RSF-based method for different n and ϵ with variable scattering coefficient (3.39) with $\rho = 1$ and $\mu_t = \mu_s + 0.2$.

n	ϵ	$T_{\text{pre}}^{\text{DIR}}$ (sec)	$T_{\text{pre}}^{\text{RSF}}$ (sec)	$T_{\text{sol}}^{\text{DIR}}$ (sec)	$T_{\text{sol}}^{\text{RSF}}$ (sec)
32	$1E{-}4$	$1.84E{+}0$	$4.26E{+}0$	$4.15E{-}2$	$1.27E{-}2$
64	$1E{-}4$	$7.58E{+}1$	$4.02E{+}1$	$6.24E{-}1$	$5.68E{-}2$
128	$1E{-}4$	–	$2.43E{+}2$	–	$2.95E{-}1$
256	$1E{-}4$	–	$1.11E{+}3$	–	$1.72E{+}0$
32	$1E{-}6$	$1.84E{+}0$	$8.34E{+}0$	$4.15E{-}2$	$1.89E{-}2$
64	$1E{-}6$	$7.58E{+}1$	$1.31E{+}2$	$6.24E{-}1$	$8.12E{-}2$
128	$1E{-}6$	–	$7.64E{+}2$	–	$4.55E{-}1$
256	$1E{-}6$	–	$3.03E{+}3$	–	$2.96E{+}0$
32	$1E{-}8$	$1.84E{+}0$	$1.01E{+}1$	$4.15E{-}2$	$2.65E{-}2$
64	$1E{-}8$	$7.58E{+}1$	$1.86E{+}2$	$6.24E{-}1$	$1.46E{-}1$
128	$1E{-}8$	–	$1.68E{+}3$	–	$7.16E{-}1$
256	$1E{-}8$	–	$5.02E{+}3$	–	$4.36E{+}0$

FFT-based method with a sufficiently small relative tolerance for GMRES if $n > 64$. Both methods work well in terms of the relative error.

Behavior for different scattering coefficients Table 9 presents the computational cost and relative error for different scattering coefficient μ_s and tolerance ϵ for the source term (2.26a). One can get the same conclusion as in the isotropic case that both the FFT-based method and RSF-based method work in the diffusive regime and the transport regime.

3.4.2. Inhomogeneous media

We test the RSF-based method for the variable transport coefficient case using two examples. The setup of the first example is that the absorption coefficient is $\mu_a = 0.2$ and the scattering term is

$$\mu_s(\boldsymbol{x})\sigma(\boldsymbol{x},\theta) = 1 + \left(2 + e^{\mathbf{i}\theta} + e^{-\mathbf{i}\theta}\right)\rho \exp\left(-\frac{|\boldsymbol{x}-\boldsymbol{c}|^2}{4}\right), \quad \boldsymbol{c} = \left(\frac{1}{2},\frac{1}{2}\right), \tag{3.39}$$

where ρ is a constant.

Table 10 and Table 11 present the computational cost and the relative error of the RSF-based method for different mesh size n and different tolerance ϵ for the scattering term (3.39) with $\rho = 1$, respectively. Table 12 presents the computational cost and relative error for different scattering coefficient ρ and tolerance ϵ for the source term (2.26a) with $n = 64$. One can see that all the conclusions for the isotropic case hold for this case.

The second example is used to study the behavior for a peaked scattering phase function. We adopt the Lorenz–Mie phase function for 2d case with the form

$$\sigma(\theta) = 4\left(1 + \frac{\cos(\theta)}{2}\right)^8 + \frac{1757}{8192}, \tag{3.40}$$

whose profile is depicted in Fig. 2. The scattering coefficient is same as that in (2.27), and the absorption coefficient is set as $\mu_a = 0.2$.

Table 13 presents the computational cost and relative error for different scattering coefficient ρ and tolerance ϵ for the source term (2.26a) with $n = 32$. One can see that the conclusions for the isotropic case also hold for this example.

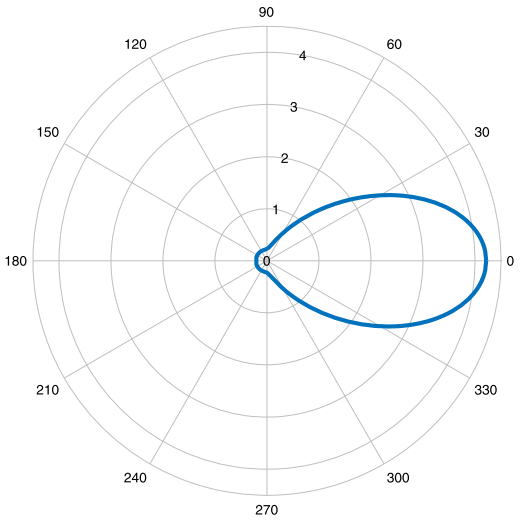

Fig. 2. Profile of Lorenz–Mie phase function (3.40).

Table 11
Anisotropic scattering case: relative error of the RSF-based method for three source terms (2.26) with variable scattering term (3.39) with $\rho = 1$ and $\mu_t = \mu_s + 0.2$. $\mathcal{E}_k$ is the relative error for the source term f_k.

n	ϵ	$\mathcal{E}_1^{\text{RSF}}$	$\mathcal{E}_2^{\text{RSF}}$	$\mathcal{E}_3^{\text{RSF}}$
32	$1E{-}4$	$4.45E{-}5$	$4.49E{-}5$	$4.01E{-}5$
64	$1E{-}4$	$1.16E{-}3$	$9.95E{-}4$	$8.94E{-}4$
32	$1E{-}6$	$2.27E{-}7$	$2.02E{-}7$	$1.65E{-}7$
64	$1E{-}6$	$6.11E{-}6$	$5.00E{-}6$	$3.53E{-}6$
32	$1E{-}8$	$1.00E{-}9$	$9.41E{-}10$	$7.88E{-}10$
64	$1E{-}8$	$1.58E{-}8$	$1.51E{-}8$	$1.28E{-}8$

Table 12
Anisotropic scattering case: computational cost and relative error for different ρ in (3.39) and ϵ with $n = 64$ and $\mu_t = \mu_s + 0.2$.

ρ	ϵ	$T_{\text{pre}}^{\text{RSF}}$	$T_{\text{sol}}^{\text{RSF}}$	$\mathcal{E}^{\text{RSF}}$
1	$1E{-}4$	$2.37E{+}1$	$7.66E{-}2$	$4.80E{-}5$
10	$1E{-}4$	$2.48E{+}1$	$7.30E{-}2$	$9.25E{-}5$
100	$1E{-}4$	$1.28E{+}1$	$4.07E{-}2$	$4.46E{-}6$
1	$1E{-}6$	$4.93E{+}1$	$1.18E{-}1$	$4.99E{-}7$
10	$1E{-}6$	$4.81E{+}1$	$1.16E{-}1$	$1.75E{-}6$
100	$1E{-}6$	$2.08E{+}1$	$5.58E{-}2$	$3.60E{-}7$
1	$1E{-}8$	$7.41E{+}1$	$1.63E{-}1$	$3.49E{-}9$
10	$1E{-}8$	$6.92E{+}1$	$1.59E{-}1$	$1.09E{-}8$
100	$1E{-}8$	$3.33E{+}1$	$6.82E{-}2$	$1.21E{-}9$

4. Conclusion

In this paper, we discussed the integral equation formulations and fast algorithms for the RTE with homogeneous and inhomogeneous media and for isotropic and anisotropic scattering. The primary observation is that a smooth scattering term can be approximated with a short convolution on unit sphere. Numerical simulations show both the FFT-based method and the RSF-based method work well. For a homogeneous medium, the FFT-based method is the method of choice due to the efficiency of the FFT. For an inhomogeneous medium, the RSF-based method requires less solution time. Moreover, numerical simulations show that the RSF-based method can be used in both transport and diffusive regimes.

To simplify the discussion, we have only studied the vacuum boundary condition and assumed that the source term f depends only on the spatial variable $\boldsymbol{x}$. The proposed algorithm remains valid for other boundary conditions and for anisotropic source terms $f(\boldsymbol{x}, \boldsymbol{v})$. As the boundary condition can be treated as a source term on the boundary, it is sufficient

Table 13
Anisotropic scattering case: computational cost and relative error of the Lorenz–Mie phase function (3.40) for different ρ and ϵ with $n = 32$ and $\mu_t = \mu_s + 0.2$.

ρ	ϵ	$T_{\text{pre}}^{\text{RSF}}$	$T_{\text{sol}}^{\text{RSF}}$	$\mathcal{E}^{\text{RSF}}$
1	$1E{-}4$	$1.06E{+}2$	$3.15E{-}1$	$2.04E{-}6$
10	$1E{-}4$	$1.84E{+}2$	$4.80E{-}1$	$1.26E{-}6$
100	$1E{-}4$	$2.04E{+}2$	$2.14E{-}1$	$1.68E{-}9$
1	$1E{-}4$	$3.16E{+}2$	$8.02E{-}1$	$2.44E{-}8$
10	$1E{-}4$	$3.63E{+}2$	$8.38E{-}1$	$1.53E{-}8$
100	$1E{-}4$	$2.83E{+}2$	$5.33E{-}1$	$1.69E{-}11$
1	$1E{-}4$	$4.50E{+}2$	$8.93E{-}1$	$3.16E{-}10$
10	$1E{-}4$	$4.76E{+}2$	$8.64E{-}1$	$2.22E{-}10$
100	$1E{-}4$	$3.29E{+}2$	$5.06E{-}1$	$1.99E{-}13$

to just treat the anisotropic source term. The only extra effort is the calculation $(\mathcal{F}\mathcal{T}^{-1} f)(\boldsymbol{x}, k)$, and this can be treated by solving

$$\begin{aligned} \boldsymbol{v} \cdot \nabla_{\boldsymbol{x}} \Phi(\boldsymbol{x}, \boldsymbol{v}) + \mu_t(\boldsymbol{x}) \Phi(\boldsymbol{x}, \boldsymbol{v}) &= f(\boldsymbol{x}, \boldsymbol{v}), \quad \text{in } \Omega \times \mathbb{S}^{d-1}, \\ \Phi(\boldsymbol{x}, \boldsymbol{v}) &= 0, \quad \text{on } \Gamma_-, \end{aligned} \tag{4.1}$$

which can be solved by existing methods, for example in [15,18].

Acknowledgements

The work of Y.F. and L.Y. is supported in part by the U.S. Department of Energy's Advanced Scientific Computing Research program under award DE-FC02-13ER26134/DE-SC0009409 and the National Science Foundation under award DMS-1521830. The authors thank Kui Ren and Yimin Zhong for constructive discussions.

References

[1] Marvin L. Adams, Paul F. Nowak, Asymptotic analysis of a computational method for time- and frequency-dependent radiative transfer, J. Comput. Phys. 146 (1) (1998) 366–403.
[2] Graham W. Alldredge, Ruo Li, Weiming Li, Approximating the $M2$ method by the extended quadrature method of moments for radiative transfer in slab geometry, Kinet. Relat. Models 9 (2) (2016) 237–249.
[3] Mohammad Asadzadeh, A finite element method for the neutron transport equation in an infinite cylindrical domain, SIAM J. Numer. Anal. 35 (4) (1998) 1299–1314.
[4] Katherine Bhan, Jerome Spanier, Condensed history Monte Carlo methods for photon transport problems, J. Comput. Phys. 225 (2) (2007) 1673–1694.
[5] K.M. Case, P.F. Zweifel, Existence and uniqueness theorems for the neutron transport equation, J. Math. Phys. 4 (11) (1963) 1376–1385.
[6] Mourad Choulli, Plamen Stefanov, An inverse boundary value problem for the stationary transport equation, Osaka J. Math. 36 (1) (1999) 87–104.
[7] Robert Dautray, Jacques-Louis Lions, Mathematical Analysis and Numerical Methods for Science and Technology: Volume 6 Evolution Problems II, Springer-Verlag, Berlin, Heidelberg, 2000.
[8] Andreas Dedner, Peter Vollmöller, An adaptive higher order method for solving the radiation transport equation on unstructured grids, J. Comput. Phys. 178 (2) (2002) 263–289.
[9] Jeffery D. Densmore, Kelly G. Thompson, Todd J. Urbatsch, A hybrid transport-diffusion Monte Carlo method for frequency-dependent radiative-transfer simulations, J. Comput. Phys. 231 (20) (2012) 6924–6934.
[10] James J. Duderstadt, William Russell Martin, Transport Theory, 1979.
[11] Herbert Egger, Matthias Schlottbom, An L^p theory for stationary radiative transfer, Appl. Anal. 93 (6) (2014) 1283–1296.
[12] Herbert Egger, Matthias Schlottbom, Stationary radiative transfer with vanishing absorption, Math. Models Methods Appl. Sci. 24 (05) (2014) 973–990.
[13] Martin Frank, Axel Klar, Edward W. Larsen, Shugo Yasuda, Time-dependent simplified P_N approximation to the equations of radiative transfer, J. Comput. Phys. 226 (2) (2007) 2289–2305.
[14] J.I. Frankel, Computational attributes of the integral form of the equation of transfer, J. Quant. Spectrosc. Radiat. Transf. 46 (4) (1991) 329–342.
[15] Hao Gao, Hongkai Zhao, A fast-forward solver of radiative transfer equation, Transp. Theory Stat. Phys. 38 (3) (2009) 149–192.
[16] William F. Godoy, Xu Liu, Parallel Jacobian-free Newton Krylov solution of the discrete ordinates method with flux limiters for 3D radiative transfer, J. Comput. Phys. 231 (11) (2012) 4257–4278.
[17] Leslie Greengard, Denis Gueyffier, Per-Gunnar Martinsson, Vladimir Rokhlin, Fast direct solvers for integral equations in complex three-dimensional domains, Acta Numer. 18 (2009) 243–275.
[18] Konstantin Grella, Ch. Schwab, Sparse tensor spherical harmonics approximation in radiative transfer, J. Comput. Phys. 230 (23) (2011) 8452–8473.
[19] Carole K. Hayakawa, Jerome Spanier, Vasan Venugopalan, Coupled forward-adjoint Monte Carlo simulations of radiative transport for the study of optical probe design in heterogeneous tissues, SIAM J. Appl. Math. 68 (1) (2007) 253–270.
[20] Kenneth L. Ho, Leslie Greengard, A fast direct solver for structured linear systems by recursive skeletonization, SIAM J. Sci. Comput. 34 (5) (2012) A2507–A2532.
[21] Kenneth L. Ho, Lexing Ying, Hierarchical interpolative factorization for elliptic operators: differential equations, Commun. Pure Appl. Math. 69 (8) (2016) 1415–1451.
[22] Kenneth L. Ho, Lexing Ying, Hierarchical interpolative factorization for elliptic operators: integral equations, Commun. Pure Appl. Math. 69 (7) (2016) 1314–1353.
[23] John K. Hunter, Bruno Nachtergaele, Applied Analysis, World Scientific Publishing Co Inc., 2001.

[24] Alexander D. Klose, Uwe Netz, Jürgen Beuthan, Andreas H. Hielscher, Optical tomography using the time-independent equation of radiative transfer—part 1: forward model, J. Quant. Spectrosc. Radiat. Transf. 72 (5) (2002) 691–713.
[25] Rainer Koch, Ralf Becker, Evaluation of quadrature schemes for the discrete ordinates method, J. Quant. Spectrosc. Radiat. Transf. 84 (4) (2004) 423–435.
[26] Thomas A. Manteuffel, Klaus J. Ressel, Gerhard Starke, A boundary functional for the least-squares finite-element solution of neutron transport problems, SIAM J. Numer. Anal. 37 (2) (1999) 556–586.
[27] Alexander Marshak, Anthony Davis, 3D Radiative Transfer in Cloudy Atmospheres, Springer Science & Business Media, 2005.
[28] Suely Oliveira, Yuanhua Deng, Preconditioned Krylov subspace methods for transport equations, Prog. Nucl. Energy 33 (1–2) (1998) 155–174.
[29] Christopher C. Paige, Michael A. Saunders, Solution of sparse indefinite systems of linear equations, SIAM J. Numer. Anal. 12 (4) (1975) 617–629.
[30] Bruce W. Patton, James Paul Holloway, Application of preconditioned GMRES to the numerical solution of the neutron transport equation, Ann. Nucl. Energy 29 (2) (2002) 109–136.
[31] Gerald C. Pomraning, The Equations of Radiation Hydrodynamics, Courier Corporation, 1973.
[32] Kui Ren, Rongting Zhang, Yimin Zhong, A fast algorithm for radiative transport in isotropic media, arXiv preprint, arXiv:1610.00835, 2016.
[33] Youcef Saad, Martin H. Schultz, GMRES: a generalized minimal residual algorithm for solving nonsymmetric linear systems, SIAM J. Sci. Stat. Comput. 7 (3) (1986) 856–869.
[34] Matthias Schlottbom, Herbert Egger, On Forward and Inverse Models in Optical Tomography, technical report, Fachgruppe Informatik, 2011.
[35] Plamen Stefanov, Gunther Uhlmann, An inverse source problem in optical molecular imaging, Anal. PDE 1 (1) (2008) 115–126.
[36] Tanja Tarvainen, Marko Vauhkonen, Ville Kolehmainen, Jari P. Kaipio, Hybrid radiative-transfer–diffusion model for optical tomography, Appl. Opt. 44 (6) (2005) 876–886.
[37] R. Turpault, M. Frank, B. Dubroca, A. Klar, Multigroup half space moment approximations to the radiative heat transfer equations, J. Comput. Phys. 198 (1) (2004) 363–371.
[38] V.S. Vladimirov, Mathematical Problems in the One-Velocity Theory of Particle Transport, technical report, Atomic Energy of Canada Limited, 1963.